TRIBHUVAN UNIVERSITY

INSTITUTE OF ENGINEERING

PULCHOWK CAMPUS

THESIS NO.: M-113-MSMDE-2023-2026

Numerical Modeling of Relativistic Jet Propagation Using Reduced-Dimensional Special-Relativistic Hydrodynamics

by

DIKSHYA KAFLE

A THESIS REPORT SUBMITTED TO THE DEPARTMENT OF MECHANICAL AND AEROSPACE ENGINEERING IN PARTIAL FULFILLMENT OF THE REQUIREMENTS FOR THE DEGREE OF MASTER OF SCIENCE IN MECHANICAL SYSTEMS DESIGN AND ENGINEERING

DEPARTMENT OF MECHANICAL AND AEROSPACE ENGINEERING

LALITPUR, NEPAL

April, 2026

COPYRIGHT

TRIBHUVAN UNIVERSITY

INSTITUTE OF ENGINEERING

PULCHOWK CAMPUS

DEPARTMENT OF MECHANICAL AND AEROSPACE ENGINEERING

LETTER OF APPROVAL

The undersigned certify that they have read, and recommended to the Institute of Engineering for acceptance, a thesis report entitled "Numerical Modeling of Relativistic Jet Propagation Using Reduced-Dimensional Special Relativistic Hydrodynamics" submitted by Dikshya Kafle in partial fulfillment of the requirements for the Degree of Master of science in Mechanical Systems Design and Engineering.

Supervisor: Asst. Prof. Kamal Darlami
Department of Mechanical and Aerospace Engineering
Institute of Engineering, Pulchowk Campus

Supervisor: Asst. Prof. Dr. Sudip Bhattrai
Department of Mechanical and Aerospace Engineering
Institute of Engineering, Pulchowk Campus

External Examiner: Arun Bikram Thapa
Assistant Professor
Department of Mechanical Engineering
Institute of Engineering, Thapathali Campus

Tribhuvan University
Institute of Engineering
Department of Mechanical and Aerospace Engineering
Pulchowk Campus

Committee Chairperson: Dr. Sudip Bhattrai
Head of the Department
Department of Mechanical and Aerospace Engineering
Institute of Engineering, Pulchowk Campus

Date of Approval: 23rd April, 2026

ABSTRACT

Special relativistic hydrodynamics (SRHD) plays a crucial role in the study of high-energy, relativistic flows characterized by strong shocks and nonlinear wave interactions. Relativistic flows do not generally admit analytical solutions hence requiring numerical solvers for simplified studies. Although several advanced SRHD solvers exist, they are often made for higher-dimensional (3D) simulations which are computationally intensive, complex to implement, and not readily accessible for educational or exploratory use, especially in simplified environments such as MATLAB. This study presents the development of a one- and two-dimensional SRHD solvers using the finite volume method with HLLE flux evaluation and MUSCL slope-limited reconstruction. The solvers were validated against standard relativistic blast wave test problems under relativistic conditions. The results demonstrate the solvers' ability to capture key flow features, including shock waves, rarefaction waves, and contact discontinuities, while also maintaining conservation properties. MUSCL reconstruction significantly reduced the numerical diffusion inherent under first-order scheme. Mesh sensitivity and CFL number analyses outlined the influence of spatial and temporal discretization on solution accuracy and stability.

The validated solvers were applied to simulate relativistic jet propagation which showed solvers' ability to capture jet features such as collimation, bow shocks, and shear layer formation. Parametric studies on Lorentz factor, density contrast, and pressure ratio highlighted their influence on jet dynamics. Simulations in high-resolution improved solution accuracy at increased computational cost. The developed solver provides a computationally efficient and reliable framework for studying relativistic flows and can be further extended to higher-order schemes and multidimensional applications.

Keywords: *Special Relativistic Hydrodynamics, HLLE, Finite-Volume Method, Newton–Raphson Method, Blast Wave, MUSCL, Courant number, Jet Propagation.*

ACKNOWLEDGEMENT

I would like to express my gratitude to my supervisors, Assistant Professor Kamal Darlami and Assistant Professor Dr. Sudip Bhattrai whose guidance, suggestions, and feedback have greatly shaped the direction and rigor of this work.

I am indebted to the Department of Mechanical and Aerospace Engineering, Pulchowk Campus, and the teaching professionals of the department for their guidance, and valuable suggestions throughout the master's program. I am also sincerely thankful to the Department for providing the resources, facilities, and institutional support essential for carrying out this research.

I would also like to appreciate all friends, seniors, and juniors who contributed directly or indirectly, whether through discussion, advice, or encouragement. Finally, I extend my deepest thanks goes to my family for their support, patience, and faith throughout my academic journey.

TABLE OF CONTENTS

LIST OF TABLES

LIST OF FIGURES

LIST OF ABBREVIATIONS

1D	One Dimensional
2D	Two Dimensional
3D	Three Dimensional
CFD	Computational Fluid Dynamics
CFL	Courant–Friedrichs–Lewy
HLLE	Harten-Lax-van Leer-Einfeldt
MUSCL	Monotonic Upstream-centered Scheme for Conservation Laws
NaN	Not a Number
SRHD	Special Relativistic Hydrodynamics
WENO	Weighted Essentially Non-Oscillatory
EOS	Equation of State

LIST OF SYMBOLS

ρ	Rest-mass density
p	Pressure
$\boldsymbol{v}$	Fluid velocity vector
v_x	Velocity components in x direction
v_y	Velocity components in y direction
c	Speed of light
W	Lorentz factor
h	Specific enthalpy
e	Specific internal energy
E	Total energy density
Γ	Adiabatic index
D	Conserved density
$\boldsymbol{S}_x$	Momentum density component in x direction
$\boldsymbol{S}_y$	Momentum density components in y direction
$\boldsymbol{S}$	Momentum density vector
τ	Energy density (excluding rest-mass energy)
$\boldsymbol{U}$	Vector of conserved variables
$\boldsymbol{V}$	Vector of primitive variables

$\boldsymbol{F}$	Flux vector
λ	Eigenvalues (wave speeds)
a	Speed of sound
Δx	Grid spacing in x direction
Δy	Grid spacing in y direction
Δt	Time step
θ	Slope limiter parameter (MUSCL)
t	Time
η	Density contrast
p_j	Pressure of the jet
p_a	Pressure of the ambient medium

1. INTRODUCTION

1.1 Background

Fluid dynamics problems involving high-speed, compressible flows exhibit strong nonlinear phenomena like shock waves, rarefaction waves and consist large gradients in flow variables. These features are commonly encountered in relativistic flows. Relativistic flows are defined as high-speed flows approaching the speed of light. As the fluid moves with the velocity closer to that of light, it undergoes relativistic effects. In such cases, unlike in classical fluid dynamics, mass, momentum and energy are no longer treated independently. They are strongly coupled and pressure and internal energy affect momentum transport. Analyzing such a flow is beyond the scope of classical fluid dynamics hence requiring extension to the classical fluid dynamic framework. The governing equations for the study of relativistic fluid flow must account for relativistic corrections to mass, momentum and energy conservation.

Some of the well-known examples of high-velocity flows are relativistic jets of astrophysical systems such as active galactic nuclei, gamma-ray bursts, microquasars, etc. They are highly energetic jets which develop complex flow structures and discontinuities during their propagation as they interact with the ambient environment.

In order to study the relativistic behaviour of the fluid, different hydrodynamic approaches are used. SRHD, GRMHD, SRMHD some of the commonly use methods. Particularly, SRHD extends the classical conservation equations of fluid dynamics to include relativistic effects. It assumes a flat space-time framework. Here the governing equations are written in conservative form and are solved using a numerical method. The analytical solutions exist only for few simplified cases, hence making the numerical modeling even more of an important tool for investigating relativistic fluid behaviour.

The three-dimensional relativistic simulations require significant computational resources. As a result, reduced-dimensional models which have lower computational cost are preferred for studying the fundamental characteristics of the relativistic flows. Such models allow detailed investigation of the evolution of flow variables and the numerical behavior of the solver.

In this study, the reduced-dimensional special relativistic hydrodynamics framework is used to model the propagation of relativistic jets into an ambient medium under different conditions resulted by varying parameters like Lorentz factor, density contrast and pressure ratio.

1.2 Special Relativistic Hydrodynamics

Special relativistic hydrodynamics is the study of fluid flow governed by conservation of mass, momentum and energy in which the velocity is close to the speed of light but never exceeds it as per the principle of special relativity.

SRHD provides a framework for describing the motion of fluids under relativistic conditions. When fluid flows reach velocities comparable to the speed of light, governing equations must be applied considering relativistic effects. In this formulation, the conservation laws of mass, momentum, and energy are modified to incorporate relativistic effects that arise from high velocities. The governing equations are typically written in conservative form so that they can be solved using numerical techniques similar to those used in computational fluid dynamics.

Unlike general relativistic models, SRHD assumes a flat spacetime and does not include gravitational effects. The magnetic fields are also neglected in the pure hydrodynamic formulation. These assumptions simplify the physical model while still allowing the main features of relativistic fluid motion to be captured.

1.3 Problem Statement

The relativistic flows are highly nonlinear, with shocks, rarefaction waves, and contact discontinuities forming as the jet interacts with the surrounding medium. Obtaining solutions for such fluid dynamics, even under SRHD, is difficult. SRHD equations alone are not capable of obtaining the solutions requiring additional support like the ideal equation of states and iterative approaches. It is difficult to study the full behavior of the relativistic flows without numerical modeling as limited analytical solutions exist.

Most existing studies are focused on three-dimensional simulations which are computationally intensive leaving reduced-dimensional solver frameworks underexplored. These are focused on

imitating astrophysical outcomes rather than the numerical methods implementation on simple, student friendly tools like MATLAB which can contribute in educational and explanatory research.

1.4 Motivation and Mechanical Engineering Relevance

Relativistic jets are typically considered in astrophysical phenomena, however, in the field of Mechanical Engineering it can be treated as a high-speed compressible flow problem. Relativistic flows involve strong nonlinearities, shock waves, and high gradients of pressure and density that are commonly studied in computational fluid dynamics (CFD) for engineering applications. Developing a robust numerical solver for such flows can help strengthen understanding of high-speed compressible fluid behavior and improve skills in numerical modeling, stability analysis, and solver implementation.

Unlike 3D models, reduced-dimensional simulations offer a practical way to explore the relativistic behaviour of the flows without requiring excessive computational resources. 1D and 2D models make it possible to test different numerical schemes, validate solvers against standard benchmark problems, and analyze how certain parameters affect flow dynamics. The entire process from solver development to the study of the effects of key parameters provides insight into relativistic fluid dynamics and at the same time reinforces concepts used in classical CFD and high-speed aerodynamics, which are central to Mechanical Engineering.

Hence, the motivation for this study is the consequence of gap in solver-focused research for relativistic flows and the provision of a link between advanced fluid dynamics problems and practical engineering analysis, which allows Mechanical Engineering students and researchers to apply familiar CFD tools to extreme flow conditions.

1.5 Objectives

1.5.1 Main Objective

To numerically model the propagation of relativistic jets using reduced-dimensional (1D and 2D) Special-Relativistic Hydrodynamics.

1.5.2 Specific Objectives

a) To formulate the conservative SRHD equations and numerical methods for numerical implementation.
b) To develop and validate a 1D SRHD numerical solver using standard relativistic test problems.
c) To extend the solver to 2D SRHD for simulating relativistic jet propagation.
d) To simulate the relativistic jet propagation into an ambient medium using the 2D solver.
e) To analyze the effects of key parameters such as Lorentz factor, density contrast, and pressure ratio on jet dynamics.

1.6 Scope of the Study

This study focuses on numerical modeling of relativistic jet propagation using reduced-dimensional SRHD. The1D solver serves as a foundation for validation as well as the solver's extension to2D. The study analyzes key flow features such as shocks, rarefaction waves, and contact discontinuity, along with the effects of parameters like Lorentz factor, density contrast, and pressure ratio.

This work is limited to reduced-dimensional SRHD models. Analysis of gravitational and magnetic effects is beyond the scope of this study. Also, a fully three-dimensional is not included. The results obtained through simulations are focused on understanding solver performance and flow dynamics rather than replicating specific astrophysical environments.

2. LITERATURE REVIEW

2.1 Relativistic Flows

Relativistic fluids are high-speed compressible fluids with strong shocks, discontinuities, rarefactions, and large gradients in flow variables and comprise highly nonlinear interactions [1, 2]. Relativistic flows typically occur in high-energy astrophysical phenomena like black hole jets, gamma-ray bursts (GRBs), supernovae, X-ray binaries, etc. They exhibit strong shocks,

rarefactions, contact discontinuities and complex interactions with the surrounding medium. Studying such complex fluid dynamics while capturing the relativistic effects is beyond the scope of classical fluid dynamics, thus requiring sophisticated, non-Newtonian computational methods like SRHD, GRMHD (General Relativistic Magnetohydrodynamics), SRMHD (Special Relativistic Magnetohydrodynamics), and related models [3,4].

In order to reproduce the physical phenomena such as jet head formation, cocoon and shock structures, most studies adapt 3D simulations [5]. Although 3D simulations capture those phenomena more accurately, the computational cost associated with them is quite high [6]. At the same time, reduced dimensional approaches i.e., 1D and 2D simulations are also capable of capturing essential features of relativistic flows including shock, discontinuities, and overall jet morphology without the need of huge resources [7].

2.2 Special Relativistic Hydrodynamics

Special relativistic hydrodynamics (SRHD) is a branch of computational fluid dynamics (CFD) that deals with fluids exhibiting relativistic properties in a relatively static ambient medium [8]. SRHD studies these relativistic fluid flows with subluminal velocities within flat Minkowski spacetime which ignores space-time curvature [1]. The flat spacetime assumption significantly simplifies the mathematical formulation by neglecting magnetic field and gravity. The SRHD follows relativistic conservation laws which is the fundamental principle of conservation of mass, momentum and energy. SRHD undergo Lorentz transformation as the equations are dependent on Lorentz factor. The governing equations of SRHD are nonlinear and hyperbolic in nature, which leads to complex wave interactions. Therefore, for obtaining the accurate numerical solution, robust numerical methods and solvers are required [9].

The SRHD equations used in this study are adopted from established sources [10–13], where their detailed formulation and derivation can be found. The system of SRHD equations is closed with an equation of state (EOS) [11, 14]. The ideal gas EOS is used, relating pressure, density, and specific enthalpy with adiabatic index.

2.3 Developments in Relativistic Hydrodynamics

Early studies on SRHD were focused on relativistic hydrodynamics code generation, formulation of modern SRHD equations, development of benchmark tests, and building advanced relativistic hydrodynamics methods. In the 1970s, James R. Wilson developed the first Eulerian SRHD code employing artificial viscosity techniques to handle shock waves, which built a foundation for the development of stable numerical simulations of high-speed flows. Gary A. Sod surveyed several finite difference methods and presented the Sod shock tube tests as a standard benchmark for validating hydrodynamic codes [15]. Martí and Müller introduced the exact Riemann solution for relativistic flows in 1994, which became a benchmark for shock tube problems [14]. Later, they also developed the first one-dimensional SRHD code employing this exact Riemann solver, establishing important standards for code validation [10]. Their comprehensive review has been updated multiple times [8,16] which further summarized high-resolution shock-capturing (HRSC) methods in SRHD. Similarly, significant contributions were made in approximate Riemann solvers and flux treatment by Schneider et al. [17] and [18] who adapted the relativistic HLLE and HLL algorithms specifically designed for SRHD, originally introduced by Harten, Lax, and van Leer (1983) for classical hydrodynamics [19]. In 1994 Toro et al. developed the HLLC solver for the Euler equations, preserving contact discontinuities [20], which Mignone and Bodo extended to relativistic flows with the aim of achieving sharper resolution of contact waves [9]. Furthermore, Mignone and Bodo presented an extension of the piecewise parabolic method to SRHD in multi-dimensions suitable for a general equation of state [21].

In the early 2000s, schemes like total variation diminishing (TVD) and essentially non-oscillatory (ENO) methods were covered [8]. Zhang and MacFadyen introduced the relativistic adaptive mesh (RAM) code, integrating fifth-order weighted essentially non-oscillatory (WENO) schemes with HLL fluxes and adaptive mesh refinement (AMR), marking the first high-order SRHD code with AMR capabilities [22]. SRHD has significantly enhanced accuracy through MUSCL (Monotonic Upstream-centered Schemes for Conservation Laws), which reduces numerical diffusion while maintaining stability near discontinuities [23]. MUSCL uses slope-limited linear reconstruction to achieve second-order spatial accuracy in smooth regions while capturing shock. In recent years the Entropy Limited Hydrodynamics (ELH) scheme also has been introduced based on the

hybridization of an unfiltered high-order scheme with the first-order Lax-Friedrichs method [24]. In 2015, Martí and Müller provided an overview of grid-based numerical methods used in relativistic hydrodynamics (RHD)and magnetohydrodynamics (RMHD) along with FORTRAN programs to compute the exact solution of the Riemann problem in RMHD and to simulate1D RMHD flows in Cartesian coordinates [3]. State-of-the-art relativistic hydrodynamics codes such as PLUTO, Athena++, and WhiskyTHC have been developed. They incorporate a variety of Riemann solvers, like HLLC, HLLE, and exact solvers combined with adaptive mesh refinement to achieve unprecedented accuracy and efficiency across a broad range of fluid dynamics regimes, including classical, special relativistic, and general relativistic hydrodynamics [25–27].

2.4 Numerical Methods for Relativistic Hydrodynamics

The numerical solvers for SRHD equations are built using the concept of numerical methods such as the finite volume method (FVM), smoothed particle hydrodynamics (SPH), the finite difference method (FDM), etc. FVM methods like the exact Riemann solver and approximate Riemann solver compute flux at the cell interface by solving local discontinuities in the flow in order to obtain numerical solutions of hyperbolic conservation laws in SRHD. Even though the exact Riemann solver provides more accuracy, it is complex, slower, and computationally expensive. The approximate Riemann solvers such as Harten, Lax, and van Leer (HLL), HLL and Contact (HLLC), and HLL and Einfeldt (HLLE), although not as accurate near shocks, are faster, simpler, and efficient and provide robust flux evaluation [14, 17, 18, 28, 29].

2.5 Reduced-Dimensional Modeling of Relativistic Flows

1D solvers are commonly used for building the foundation of the solver for future extensions. They work as validation tool against standard test problems such as shock tubes and blast wave test. Once validated, the 1D solver can be extended to 2D for studying relativistic jet propagation scenarios, including jet penetration, shock positions, mixing layers, and interactions with ambient medium.

Reduced-dimensional modeling handles detailed investigation of numerical methods, solvers stability as well as parameter study all while avoiding the computational cost associated with 3D modeling [3, 4].

2.6 Research Gap and Motivation

In relativistic hydrodynamics, while many studies seem to focus on physical outcomes of the solvers, only few studies undergo solver development, validation and extension of 1D solver in to 2D [8, 10]. Most works are prioritized into astrophysical applications compared to numerical method analysis, and CFD applications hence leaning to 3D modeling [6]. This has created a gap in reduced dimensional SRHD research.

In the field of Mechanical Engineering, relativistic jets can be treated as high-speed compressible flows, which allow the application of CFD techniques to study extreme fluid behavior. Developing and validating 1D and 2D SRHD solvers provides a platform to understand relativistic fluid dynamics as well as solver's performance, numerical stability, and the effects of key parameters [10].

3. METHODOLOGY

3.1 Methodological Framework

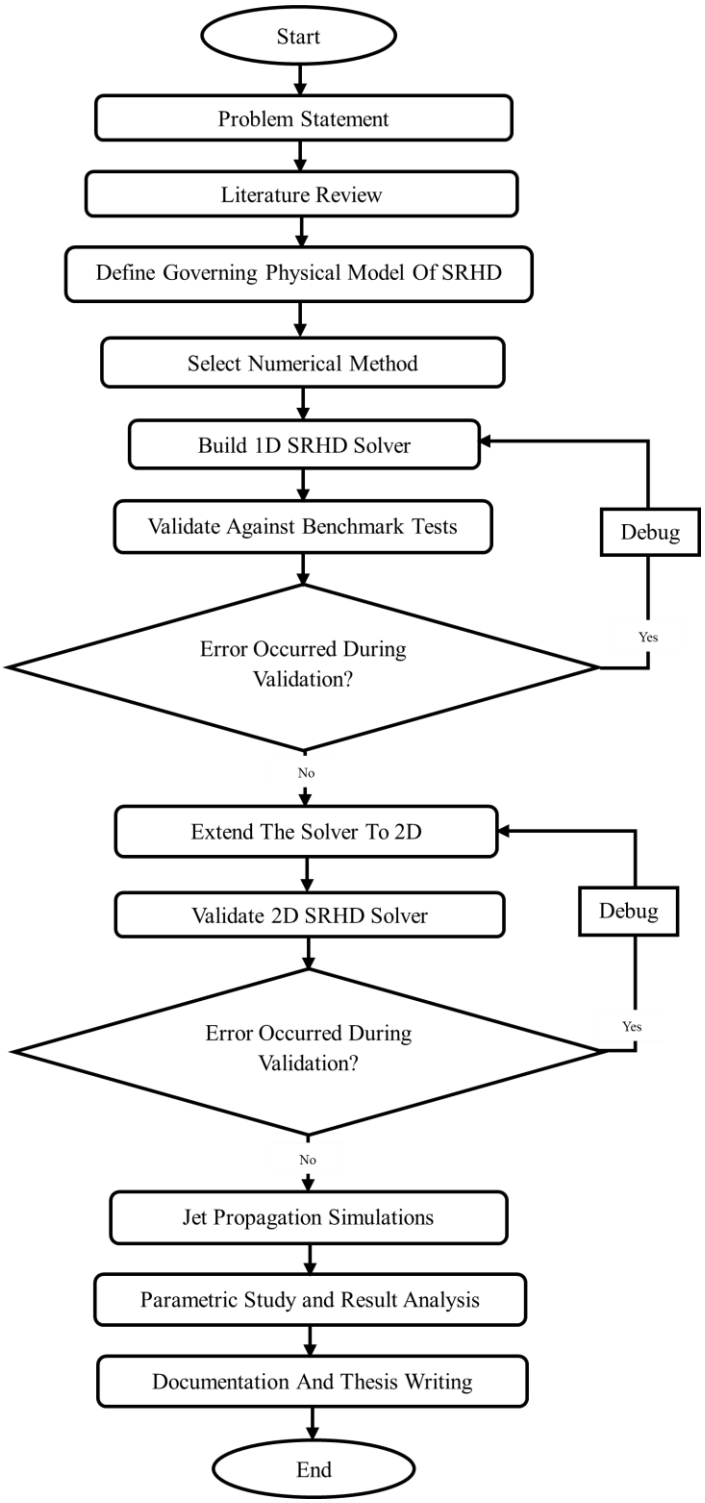

Figure 1: Methodology

This research, aimed to study relativistic jet propagation, followed a systematic pattern beginning with the formulation of problem statement, followed by an extensive literature review of SRHD and numerical solution techniques. With that the governing physical model of SRHD was defined along with selection of appropriate numerical method, primarily FVM with HLLE, an approximate Riemann solver. The computational implementation of the methodology was carried out in MATLAB. The numerical method was applied with first and second order reconstruction while building 1D SRHD solver. The developed solver was then validated against standard, benchmark tests provided by Marti and Muller through their research. Among first-order and second-order reconstruction, one fitting reconstruction approach was elected to move forward with the expansion of the solver into two dimensions.

The validated 2D solver was further adjusted and adapted for the simulation of 2D relativistic circular blast wave and jet propagation. After post-processing and result analysis, the research was concluded with documentation and thesis writing.

3.2 Governing Equations and Physical Model for SRHD

The 1D and 2D SRHD equations, closed by ideal gas equation of state, are formulated to show the evolution of ideal relativistic fluid in Minkowski (flat) spacetime neglecting gravity, the magnetic field and viscosity.

3.2.1 Primitive Variables

In SRHD primitive variables are the fundamental quantities which describe the relativistic fluid behaviour. They tell what the fluid is like at a point. They are:

Density: ρ

Pressure: p

Velocity components: v_x, v_y

In 1D,

$$v_y = 0$$

$$\therefore v^2 = v_x^2$$

3.2.2 Auxiliary Variables

The auxiliary variables are necessary for converting primitive variables to conserved variables and computing fluxes in the solver.

Lorentz factor:

It describes the relativistic effects that appear when the fluid moves at speeds close to the speed of light.

$$W = \frac{1}{\sqrt{1 - v^2}} \quad \ldots(1)$$

Specific enthalpy:

It represents the total energy content of the fluid, including rest-mass energy and internal energy. It is given by ideal gas EOS,

$$p = (\Gamma - 1)\rho\epsilon \quad \ldots(2)$$

Where,

Specific internal energy,

$$\epsilon = \frac{p}{(\Gamma - 1)\rho} \quad \ldots(3)$$

Also,

Specific enthalpy,

$$h = 1 + \epsilon + \frac{p}{\rho} \quad \ldots(4)$$

$$\therefore h = 1 + \frac{\Gamma}{\Gamma - 1}\frac{p}{\rho} \quad \ldots(5)$$

Where,

Γ = adiabatic index (5/3, 4/3)

3.2.3 Conserved Variables

Primitive variables like density, velocity, and pressure are converted into conserved variables to ensure the conservation of mass, momentum, and energy even across shocks and discontinuities. This conversion is essential for stable and accurate computation of fluxes in the solver. While primitive variables describe only the local state of a fluid, conserved variables show how much of mass, momentum, and energy exists per unit volume, and how it flows in space.

$$\boldsymbol{U} = \begin{bmatrix} D \\ S_x \\ S_y \\ \tau \end{bmatrix} = \begin{bmatrix} \rho W \\ \rho h W^2 v_x \\ \rho h W^2 v_y \\ \rho h W^2 - p - \rho W \end{bmatrix} \quad \ldots(6)$$

Where:

D is Conserved rest-mass density

S_x and S_y are x and y components of conserved momentum density

τ is conserved energy density (internal + kinetic energy)

In 1D: $S_y = 0$

3.2.4 Conservative Form Of SRHD

The primitive variables (ρ, v, p) do not ensure conservation in numerical computations, hence the governing equations are expressed in conservative form to accurately capture those features. The equation describes how mass, momentum, and energy evolve with time in the computational domain. The change within a control volume occurs due to the flux of these quantities across the cell boundaries.

In 2D:

$$\frac{\partial \boldsymbol{U}}{\partial t} + \frac{\partial \boldsymbol{F}(\boldsymbol{U})}{\partial x} + \frac{\partial \boldsymbol{G}(\boldsymbol{U})}{\partial y} = 0 \quad \ldots(7)$$

where,

F(U) = flux in *x* direction

G(U) = flux in *y* direction

In 1D:

$$\frac{\partial \boldsymbol{U}}{\partial t} + \frac{\partial \boldsymbol{F}(\boldsymbol{U})}{\partial x} = 0 \qquad \ldots(8)$$

3.2.5 Equation Of State

The system of SRHD equations is closed with an equation of state (EOS). The ideal gas EOS is used, relating pressure, density, and specific enthalpy with adiabatic index as given by Equation 5.

3.3 Numerical Methods

3.3.1 Finite Volume Method

FVM is an excellent numerical method with an inherent conservation feature used to solve SRHD equations. Under FVM, the governing equations are written in integral (conservative) form and the computational domain is discretized into a series of control volumes (cells). The evolution of the conserved variables in each cell is determined by the net fluxes entering and leaving through the cell interfaces. This flux-based formulation ensures strict conservation of mass, momentum, and energy at the discrete level, making it particularly suitable for relativistic hydrodynamic simulations involving discontinuities.

3.3.2 Fluxes

In SRHD, flux represents the quantity of mass, momentum, or energy that flows through the boundary of a small control volume.

Mass flux:

It gives the amount of mass that crosses the interface between two neighbouring computational cells per unit time.

Along x-direction; …(9)

$$\boldsymbol{F}_D = Dv_x$$

Along y-direction;

$$\boldsymbol{G}_D = Dv_y \quad \ldots(10)$$

Momentum:

Along x-direction;

$$\boldsymbol{F}_{S_x} = S_x v_x + p \quad \ldots(11)$$

$$\boldsymbol{G}_{S_x} = S_x v_y \quad \ldots(12)$$

Along y-direction;

$$\boldsymbol{F}_{S_y} = S_y v_x \quad \ldots(13)$$

$$\boldsymbol{G}_{S_y} = S_y v_y + p \quad \ldots(14)$$

Energy:

Along x-direction;

$$\boldsymbol{F}_\tau = \tau v_x + p v_x \quad \ldots(15)$$

Along y-direction;

$$\boldsymbol{G}_{\boldsymbol{\tau}} = \tau v_y + p v_y \quad \ldots(16)$$

1D analogue: Only *x*-direction fluxes used.

3.3.3 HLLE Approximate Riemann Solver

The HLLE solver is an approximate Riemann solver used to compute the numerical flux at the interface between neighbouring computational cells. It estimates the propagation of waves generated by discontinuities in the flow without solving the full Riemann problem exactly. This method is widely used in relativistic hydrodynamics as it provides robustness, simplicity, and also has the ability to capture shocks and discontinuities in a stable manner. Moreover, it avoids the complexity of exact Riemann solvers, making it computationally efficient and suitable for relativistic flow simulations.

The HLLE solver computes numerical fluxes at cell interfaces using left and right primitive states. To estimate wave propagation in relativistic flows, it requires the following:

Relativistic sound speed:

It determines how fast small pressure disturbances propagate through the fluid.

$$c_s = \sqrt{\frac{\Gamma p}{\rho h}} \qquad \ldots(17)$$

Characteristic speeds along x and y directions:

The wave speeds λ represent the fastest and slowest speeds at which information (mass, momentum, energy) can travel through the fluid along a given direction locally. These speeds combine the fluid velocity and the sound speed, so they determine how quickly the effects of a change in one cell influence neighbouring cells.

$$\lambda_x^{\pm} = \frac{v_x \pm c_s}{1 \pm v_x c_s} \qquad \ldots(18)$$

$$\lambda_y^{\pm} = \frac{v_y \pm c_s}{1 \pm v_y c_s} \qquad \ldots(19)$$

Fastest signal speeds:

These are the bracketed signal speeds used by the HLLE solver. They are computed from the λ values on both sides of a cell interface to represent the slowest and fastest signals that could affect the interface. They ensure that all possible signals (mass, momentum, energy) are captured at the interface.

In *x*-direction,

$$a_-^x = \min\left(\lambda_{x,L}^-, \lambda_{x,R}^-, 0\right) \qquad \ldots(20)$$

$$a_+^x = \max\left(\lambda_{x,L}^+, \lambda_{x,R}^+, 0\right) \qquad \ldots(21)$$

In *y*-direction,

$$a_{-}^{y} = \min\left(\lambda_{y,L}^{-}, \lambda_{y,R}^{-}, 0\right) \quad \ldots(22)$$

$$a_{+}^{y} = \max\left(\lambda_{y,L}^{+}, \lambda_{y,R}^{+}, 0\right) \quad \ldots(23)$$

HLLE flux:

The HLLE flux at a cell interface is computed using the fastest left and right-going signal speeds (a_- and a_+) and the conserved variables on the left and right sides. It provides an approximate solution to the Riemann problem by averaging the fluxes and accounting for wave propagation without solving the full problem exactly.

The HLLE flux in the x and y directions are given by:

$$\boldsymbol{F}_{HLLE} = \frac{a_+ \boldsymbol{F}_L - a_- \boldsymbol{F}_R + a_+ a_- (\boldsymbol{U}_R - \boldsymbol{U}_L)}{a_+ - a_-} \quad \ldots(24)$$

and,

$$\boldsymbol{G}_{HLLE} = \frac{a_+ \boldsymbol{G}_L - a_- \boldsymbol{G}_R + a_+ a_- (\boldsymbol{U}_R - \boldsymbol{U}_L)}{a_+ - a_-} \quad \ldots(25)$$

In 1D: Only *x*-direction interface flux ($\boldsymbol{F}_{HLLE}$) is used.

3.3.4 CFL Condition

The Courant–Friedrichs–Lewy (CFL) condition determines the time step in the numerical simulation. It ensures numerical stability by restricting how far information can travel during a single time step. The execution of CFL is done to ensure that the waves or signals will not move across more than one computational cell in one time step. The CFL condition therefore controls the maximum allowable time step based on the largest signal (wave) speed in the computational domain. For stability, the Courant number must be kept less than 1, ensuring that the numerical method remains stable and accurately captures wave propagation.

The time step is given by:

2D:

$$\Delta t = CFL \times min\left(\frac{\Delta x}{a_{max}}, \frac{\Delta y}{a_{max}}\right) \quad \ldots(26)$$

1D:

$$\Delta t = CFL \times \frac{\Delta x}{a_{max}} \quad \ldots(27)$$

Where:

$a_{\max} = max(0,\ a_{-}, a_{+})$ over all interfaces (largest wave speed)

CFL < 1 (for stability)

Δx= cell width in *x*-direction

Δy= cell spacing in *y*-direction

In two-dimensional simulations, the time step must satisfy the stability condition in both spatial directions, which is why the minimum value between the *x* and *y* directions is chosen.

3.3.5 Finite-Volume Time Update

In the finite-volume method, the conserved variables in each computational cell are updated by accounting for the net flux of conserved quantities across the cell interfaces during a time step. The change in the conserved quantity within a cell is determined by the difference between incoming and outgoing fluxes through its boundaries. This ensures that the conservation of mass, momentum, and energy is maintained in the numerical scheme.

2D:

$$\boldsymbol{U}_{i,j}^{n+1} = \boldsymbol{U}_{i,j}^{n} - \frac{\Delta t}{\Delta x}(\boldsymbol{F}_{i+1/2,j} - \boldsymbol{F}_{i-1/2,j}) - \frac{\Delta t}{\Delta y}(\boldsymbol{G}_{i,j+1/2} - \boldsymbol{G}_{i,j-1/2}) \quad \ldots(28)$$

1D:

$$\boldsymbol{U}_{i}^{n+1} = \boldsymbol{U}_{i}^{n} - \frac{\Delta t}{\Delta x}(\boldsymbol{F}_{i+1/2} - \boldsymbol{F}_{i-1/2}) \quad \ldots(29)$$

Here:

$\boldsymbol{U}^n$ = conserved variables at the current time step

$\boldsymbol{U}^{n+1}$ = conserved variables at the next time step

$\boldsymbol{F}$, $\boldsymbol{G}$ = numerical fluxes in the x and y directions

i, j = indices of the computational cell

3.3.6 Primitive Variable Recovery Through Newton–Raphson Iteration

As the SRHD equation is non-linear, the primitive variables cannot be obtained explicitly from the conserved variables. Therefore, a Newton–Raphson iterative method is used to recover the pressure. Once the pressure is obtained, the remaining primitive variables such as density and velocity are computed from the conserved quantities.

Residual function for pressure:

$$f(p) = \rho h W^2 - \tau - p - D = 0 \qquad \ldots(30)$$

Define unknown:

$$p = p^{(k)}$$

Newton–Raphson iteration:

$$p^{(k+1)} = p^{(k)} - \frac{f(p^{(k)})}{f'(p^{(k)})} \qquad \ldots(31)$$

3.3.7 Derivatives for Newton–Raphson Iteration (1D Case)

Velocity derivative:

$$v = \frac{S}{\tau + p + D}$$

$$\frac{dv}{dp} = -\frac{S}{(\tau+p+D)^2} \qquad \ldots(32)$$

Lorentz factor derivative:

$$W = (1 - v^2)^{-1/2}$$

$$\frac{dW}{dp} = vW^3 \frac{dv}{dp} \qquad \ldots(33)$$

Density derivative:

$$\rho = \frac{D}{W}$$

$$\frac{d\rho}{dp} = -\frac{D}{W^2}\frac{dW}{dp} \quad \ldots(34)$$

Specific enthalpy derivative:

$$h = 1 + \frac{\Gamma}{\Gamma - 1}\frac{p}{\rho}$$

$$\frac{dh}{dp} = \frac{\Gamma}{\Gamma - 1}\left(\frac{1}{\rho} - \frac{p}{\rho^2}\frac{d\rho}{dp}\right)$$

$$\frac{dh}{dp} = \frac{\Gamma}{\Gamma - 1}\left(\frac{1}{\rho} + \frac{p}{\rho W}\frac{dW}{dp}\right) \quad \ldots(35)$$

Derivative of residual function:

$$f(p) = \rho h W^2 - (\tau + p + D)$$

$$\frac{df}{dp} = \mathrm{D}\left(h\frac{dW}{dp} + W\frac{dh}{dp}\right) - 1 \quad \ldots(36)$$

3.3.8 Convergence Check

Convergence is declared when the relative change in pressure between successive iterations becomes smaller than a prescribed tolerance. The Newton–Raphson iterations continue until:

$$\left|\frac{p^{(k+1)} - p^{(k)}}{p^{(k+1)}}\right| < \varepsilon \quad \ldots(37)$$

Where,

ε (tolerance) = 1e-9, was taken for this study.

3.3.9 Spatial Reconstruction Scheme

In its simplest form, the solution in each cell is assumed piecewise constant, resulting in a first-order scheme. Even though stable, the solution may suffer from excessive numerical diffusion, which smears sharp discontinuities such as shock waves and contact discontinuities. To improve

the spatial accuracy and reduce the smearing, MUSCL is employed as a higher-order reconstruction technique in this work. In MUSCL, instead of assuming a constant value within each cell, a linear variation of the primitive variables is reconstructed inside each cell. The left and right states at the interface i+1/2 are computed as:

$$\boldsymbol{V}^{L}_{i+\frac{1}{2}} = \boldsymbol{V}_i + \frac{1}{2}\,\phi(\Delta \boldsymbol{V}_i) \quad \ldots(38)$$

$$\boldsymbol{V}^{R}_{i+\frac{1}{2}} = \boldsymbol{V}_{i+1} - \frac{1}{2}\,\phi(\Delta \boldsymbol{V}_{i+1}) \quad \ldots(39)$$

Where $\boldsymbol{V}_i$ represents the cell-averaged primitive variable vector in cell i, $\Delta \boldsymbol{V}_i = \boldsymbol{V}_{i+1} - \boldsymbol{V}_i$, and ϕ is a slope limiter function used to prevent spurious oscillations near discontinuities. The reconstructed interface states $\boldsymbol{V}^{L}_{i+\frac{1}{2}}$ and $\boldsymbol{V}^{R}_{i+\frac{1}{2}}$ are then used as inputs to the HLLE Riemann solver. By employing MUSCL reconstruction, the scheme achieves second-order accuracy in smooth regions, while the slope limiter ensures monotonicity near shocks, effectively reducing numerical diffusion without introducing non-physical oscillations.

3.4 Solver Development

3.4.1 1D SRHD Solver

The development of the numerical solver began with the implementation of one-dimensional Special Relativistic Hydrodynamics (SRHD) (Equation 8) in MATLAB. The solver was formulated in conservative form and implemented using a finite-volume framework on a uniform computational grid. All the 1D equivalent equations from conversion of primitive variables followed by HLLE flux to primitive variables recovery were incorporated into the solver for the building up of the 1D SRHD solver. Both first and second order reconstructions were applied separately into the solver with the aim of achieving spatial accuracy.

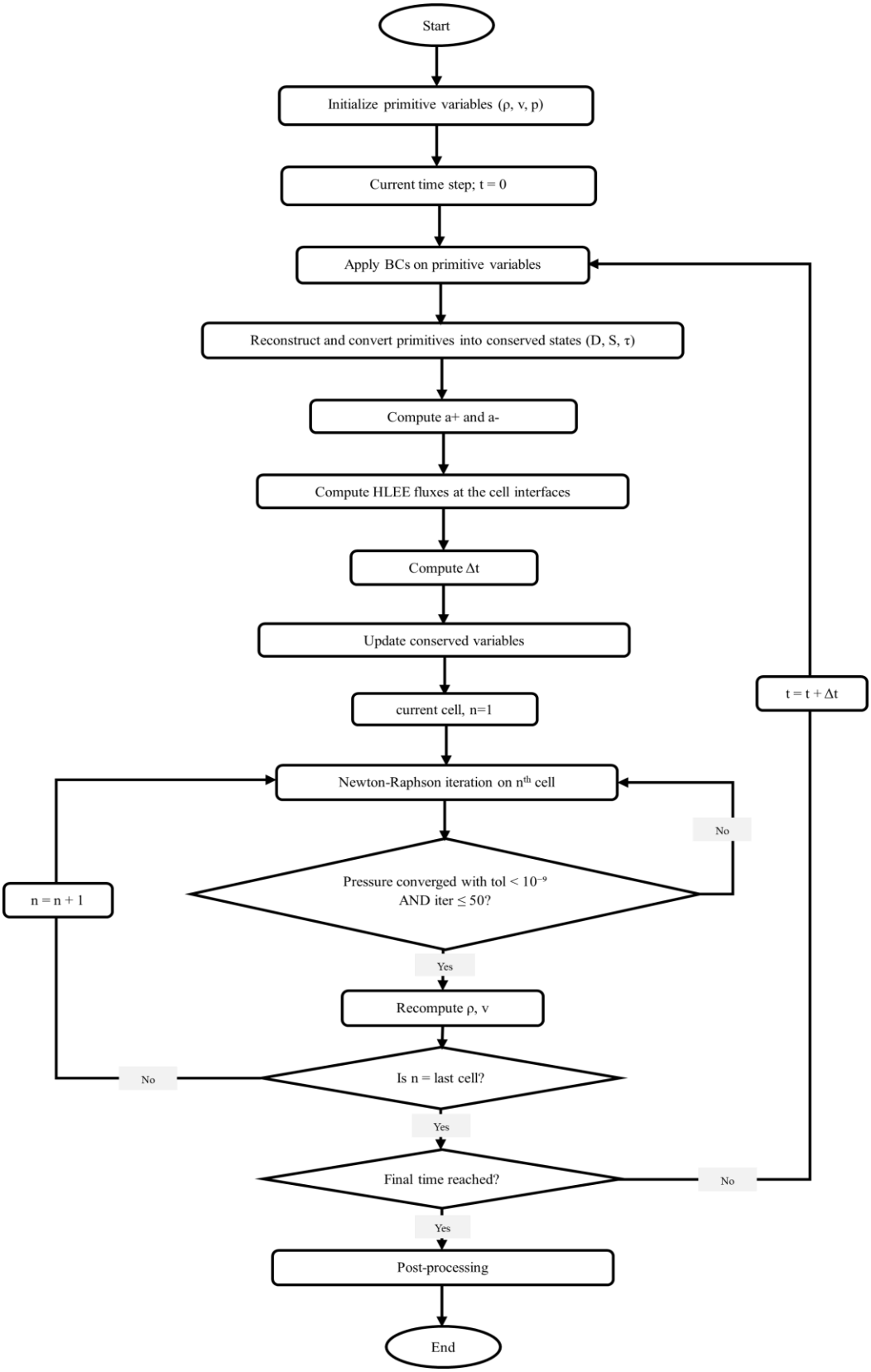

Figure 2: Flowchart of the SRHD solver algorithm.

The 1D solver developed in MATLAB utilizes a cell-wise finite volume formulation and follows a structured computational procedure from initialization of primitive variables to their recovery, as illustrated in flowchart from Figure 2. The solution begins with the initialization of primitive variables (ρ, v, p) over a non-dimensionalized computational domain. As the time-stepping loop starts, boundary conditions (BCs) are applied to the primitive variables for the treatment of ghost cells. The primitive variables in the physical cells are then transformed into conserved variables (D, S, τ) to evolve the system using the conservative SRHD equations. In case of the solver using MUSCL reconstruction, only after being reconstructed through slope limiting approach are the primitive variables transformed into conserved states. Based on the left and right conserved states and the fastest left- and right-going wave speeds (a^+, a^-), the HLLE fluxes are computed at each cell interface. The time step Δt is updated using an appropriate Courant number, and the conserved variables are subsequently updated in each cell using the finite volume formulation. The conserved variables update is followed by primitive variables recovery through the Newton-Raphson iterative method, solving the nonlinear relationship between conserved and primitive variables. A pressure residual function is used for the iteration process, which is run for each cell. When the pressure has finally converged within the preset tolerance and iteration, other primitive variables, density and velocity, are also recovered. The recovered primitives are set as the initial guess for the next cell, and the iteration continues till the last cell. This process from applying BCs to recovering primitive variables persists for each time step until the final time specified for simulation is reached.

3.4.2 2D SRHD Solver

The 1D solver after its validation was extended to second dimension using 2D equivalent equations of SRHD, HLLE flux, and finite volume update. While 1D solver presented computational scope of both piece wise constant and the MUSCL reconstruction, 2D solver was build using only MUSCL reconstruction with slope limiting to ensure high-order spatial accuracy. The 2D SRHD solver follows the same overall computational algorithm as the 1D solver, demonstrated by the flowchart in Figure 2.

3.5 Validation Techniques

To check if the developed solvers actually solve the equations and produce physically reliable solutions free of numerical artifacts, they were tested against Martí and Müller's standard

relativistic blast wave tests cases [8]. The validation stage plays a crucial role in ensuring solver's integrity, robustness, accuracy, reliability, and their ability to capture shocks, discontinuities, rarefactions and the relativistic behaviours.

3.5.1 Relativistic Blast Wave Tests

The developed 1D and 2D SRHD solvers underwent simulation for the initial conditions taken from Marti and Muller's relativistic blast wave Test-1 and Test-2. The numerical solutions obtained from the application of these standard test cases were compared to the exact solutions of the same, in order to assess the numerical stability, robustness and accuracy of the developed solvers.

3.5.2 Relativistic Circular Blast Wave

This particular test case was implemented solely to 2D SRHD solver, as it features a central high-pressure region which generates a strong shock wave that expands radially outward into the ambient medium. Relativistic circular blast wave simulation is particularly useful to assess the solver's capacity to capture multi-dimensional shock propagation and accurately maintain radial symmetry.

3.5.3 Error Norms

To quantitatively evaluate the accuracy of the solvers, the difference between the numerical and reference solutions was computed using standard error norms.

Three error measures were considered:

L_1 norm: average absolute error across the domain.
L_2 norm: root mean square error across the domain.
$L\infty$ norm: maximum absolute error

$$L_1 = \sum_{i,j} | u_{i,j}^{\text{num}} - u_{i,j}^{\text{exact}} | \Delta x \Delta y \quad \ldots(40)$$

$$L_2 = \sqrt{\sum_{i,j} (u_{i,j}^{\text{num}} - u_{i,j}^{\text{exact}})^2 \Delta x \Delta y} \quad \ldots(41)$$

$$L_\infty = \max | u_{i,j}^{\text{num}} - u_{i,j}^{\text{exact}} | \quad \ldots(42)$$

Relatively small error values are desired to indicate that the solver accurately reproduces the benchmark solution.

4. RESULTS AND DISSCUSION

4.1 1D SRHD Solver Validation

The 1D SRHD solver with the HLLE flux scheme was applied for uniform grids of 400 cells, Courant number 0.4, and final time step 0.4. The adiabatic index was set as $\Gamma = 5/3$, corresponding to an ideal relativistic fluid in mildly relativistic regime. The initial discontinuity was placed at the center ($x = 0.5$) of the computational domain [0,1] with zero-gradient (outflow) boundary conditions imposed on both ends. The initial conditions were taken from benchmark tests, proposed by Martí and Müller as relativistic blast wave problems, Test-1 and Test-2 for the validation of the developed solver.

Test-1:

Left state: $\rho = 10$, $v = 0$, $p = 13.33$

Right state: $\rho = 1$, $v = 0$, $p = 10^{-6}$

Test-2:

Left state: $\rho = 1$, $v = 0$, $p = 1000$

Right state: $\rho = 0.1$, $v = 0$, $p = 0.01$

4.1.1 Conservation Verification

In the developed 1D SRHD solver the initial conditions from relativistic blast wave Test-1 were applied. To verify if the solver follows the relativistic conservation law, the total mass, total momentum, and total energy deviations over time were monitored throughout the simulation. Figure 3. Shows the relative drift in mass remained at around machine precision of order 10^{-16}, which indicates excellent mass conservation properties of the finite volume formulation. The small oscillations observed in the mass conservation arise from floating-point round-off errors and accumulation of numerical flux differences and are therefore negligible.

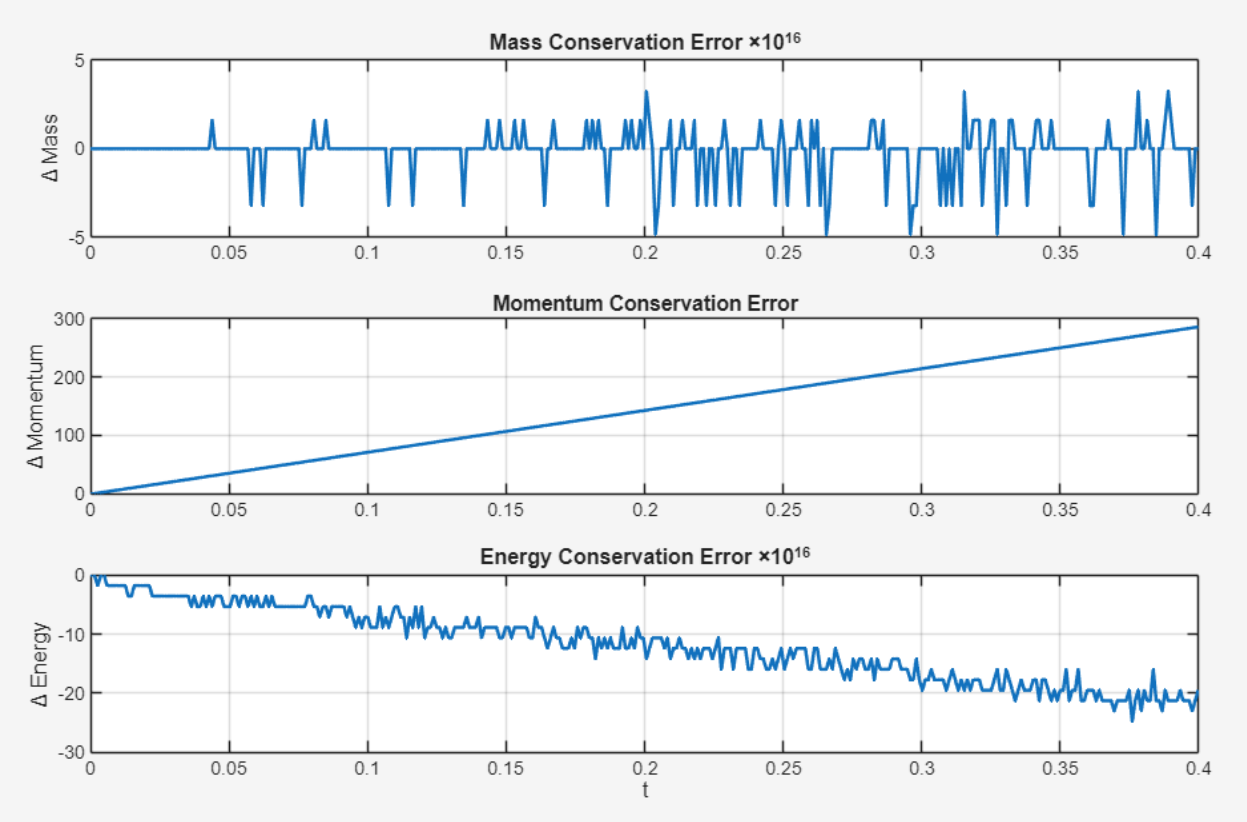

Figure 3: Conservation error over time.

Similarly, the total energy shows a very small systematic drift of order 10^{-16}. This behavior can be attributed to numerical dissipation inherent in the HLLE flux, truncation errors from the first-order spatial reconstruction, and iterative errors introduced during primitive variable recovery. The overall energy conservation remains within acceptable numerical limits. Unlike mass and energy, momentum shows a small linear increase over time. This behavior does not indicate a violation of conservation as it is resulted by the use of outflow boundary conditions. The computational domain is effectively open and the momentum can leave the domain through the boundaries, leading to a net change in total momentum. The overall conservation analysis confirms that the implemented finite volume scheme maintains the relativistic conservation laws to a high degree of accuracy.

4.1.2 Solver Validation Against Benchmark Test Problems

Figure 4 displays the primitive variables profile generated by the numerical solver which is compared with the reference solutions of the benchmark test problems, relativistic blast wave

problems, Test-1 (top panel) and Test-2 (bottom panel). Test-1 incorporates moderate relativistic conditions while Test-2 consists of strong relativistic conditions

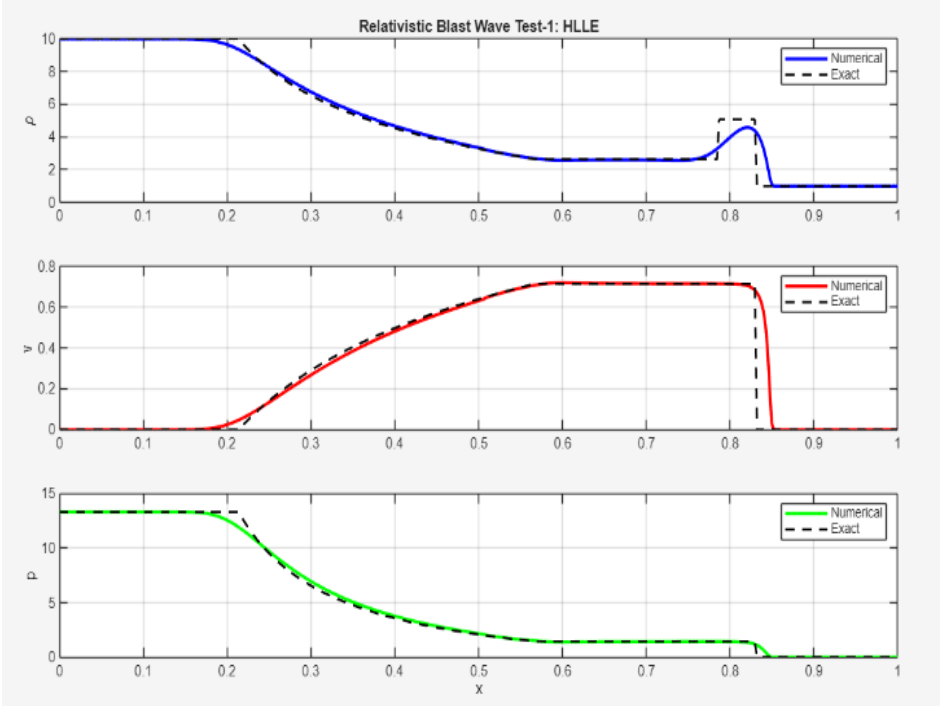

a) Test-1

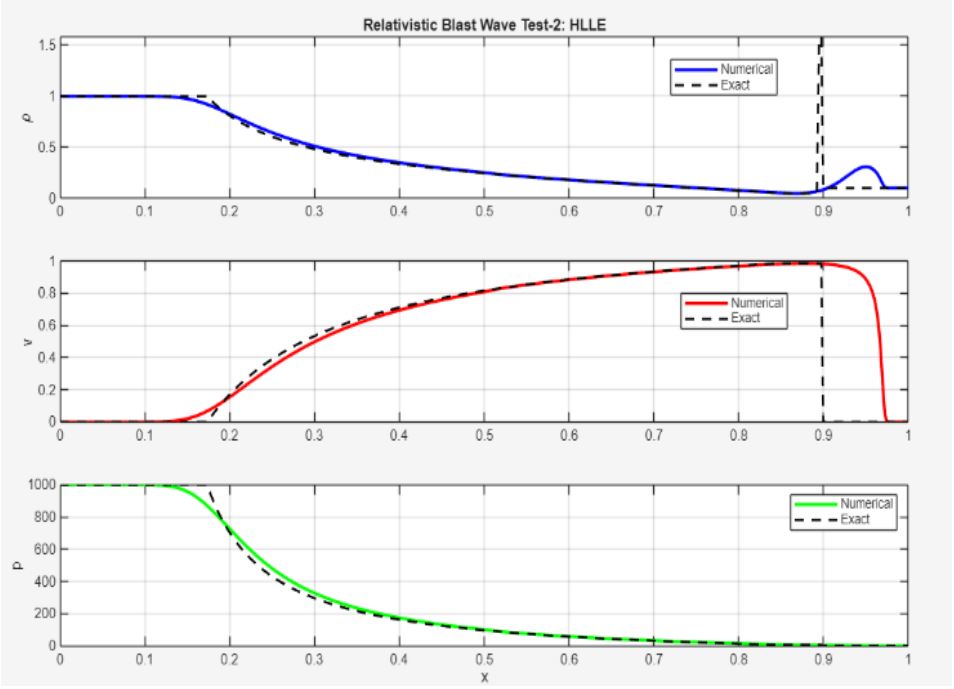

b) Test-2

Figure 4: Primitive variable profiles for Special Relativistic Blast Wave Test-1 and Test-2.

Both the test problems consist of a left-going rarefaction and a right-moving shock, arising from the strong initial pressure discontinuity that drives expansion into the low-pressure region and shock propagation toward the high-pressure region. Also, a contact discontinuity appears between the shock and rarefaction, resulting from the rest-mass density being a freely advected quantity, unlike momentum and energy, which enforce continuity of pressure and velocity. However, Test-2 represents a more challenging scenario with strong pressure gradients (initial pressure ratio, p_L/p_R = 105). Under such condition, relativistic effects become more pronounced and the solution significantly more sensitive to numerical diffusion as can be seen in Figure 4(b).

The numerical solutions of the solver are in good agreement with the reference solutions, hinting at the solver's accuracy. This agreement is further supported by the error norms presentped in Table 1, providing quantitative evidence of the solver's ability to accurately capture the key features of relativistic blast waves across both moderate and strong test cases.

Table 1: Error norms for first-order (piecewise constant) reconstruction for Test-1 and Test-2.

Tests	**Error Norms**	ρ	v	p
Test-1	L_1	1.522e-01	1.577e-02	1.211e-01
	L_2	3.951e-01	7.307e-02	2.475e-01
	$L\infty$	3.235e+00	6.701e-01	1.369e+00
Test-2	L_1	2.497e-02	7.397e-02	1.121e+01
	L_2	1.137e-01	2.407e-01	2.272e+01
	$L\infty$	1.506e+00	9.821e-01	1.272e+02

However, due to the first-order spatial reconstruction, the solution exhibits significant numerical diffusion. This is particularly evident near the contact discontinuity and shock front, where the density and pressure profiles are noticeably smeared over several grid cells. The HLLE solver, being inherently diffusive, further contributes to the broadening of discontinuities, especially in regions with steep gradients. As a result, peak values in density and pressure are slightly under-predicted, and the contact surface is poorly resolved. The velocity profile shows comparatively better agreement with the exact solution peak values, as it is less sensitive to diffusive effects than density and pressure. The numerical diffusion due to first-order reconstruction motivated the use

of a second-order reconstruction scheme in order to enhance the solver's capacity of solving 1D SRHD problems.

4.1.3 MUSCL Reconstruction

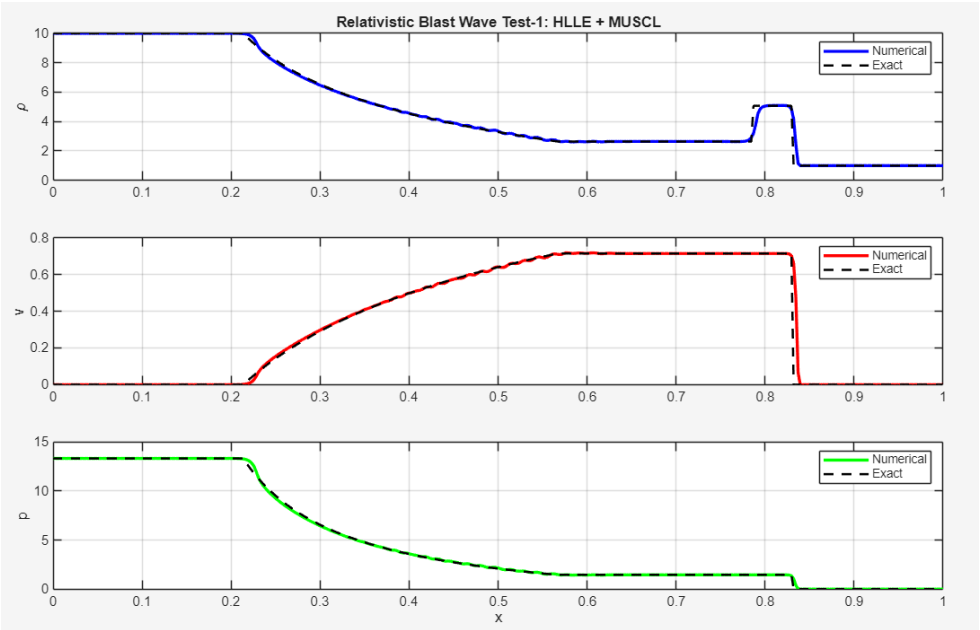

a) Test-1

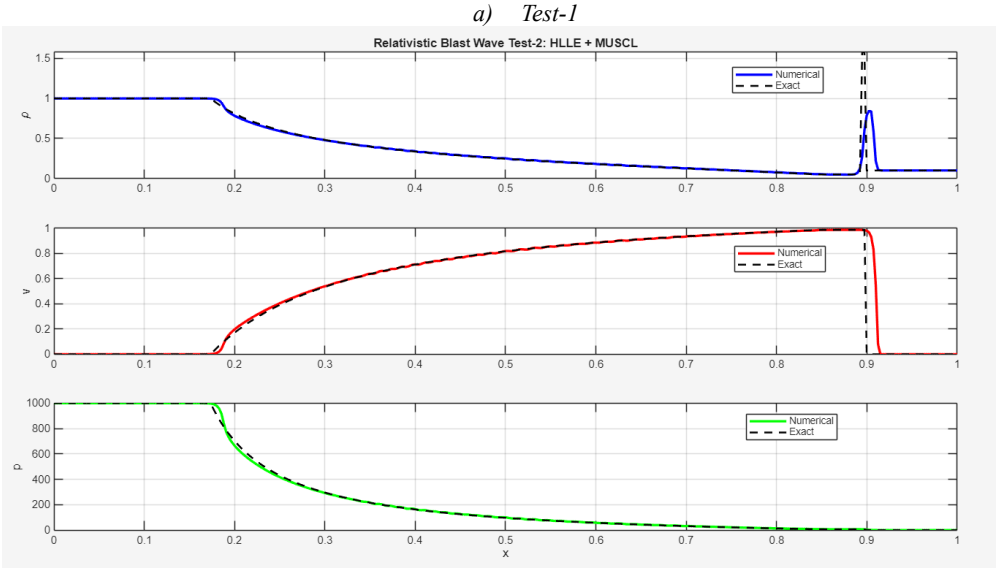

b) Test-2

Figure 5: Primitive variable profiles for Special Relativistic Blast Wave Test-1 and Test-2 with MUSCL (slope-limited) reconstruction.

The limitations of first-order reconstruction were addressed by incorporating MUSCL with a slope-limiting approach. It enabled more accurate estimation of left and right states at the cell interface by reconstructing piecewise linear profiles within each computational cell. Compared to the primitive variable profile from Figure 4 without MUSCL reconstruction, the profiles from

Figure 5 seem to have maintained stability near discontinuities, resolved the gradients more precisely, and captured the rarefaction, shock and contact discontinuity better by lowering the spurious oscillations due to the incorporation of MUSCL reconstruction.

Table 2: Error norms for Test-1 and Test–2 based second-order reconstruction.

Tests	**Error Norms**	ρ	v	p
Test-1	L_1	4.480e-02	4.999e-03	3.681e-02
	L_2	2.162e-01	4.112e-02	1.067e-01
	$L\infty$	3.172e+00	6.619e-01	1.045e+00
Test-2	L_1	1.617e-02	1.411e-02	3.515e+00
	L_2	1.063e-01	9.734e-02	1.030e+01
	$L\infty$	1.306e+00	9.794e-01	8.529e+01

Error norms in Table 2 show reduced errors, as the application of MUSCL led to overall improvement in the quality of numerical solutions for both the test cases with improved alignment with reference profiles. Furthermore, Table 3 shows that the errors significantly decreased for all primitive variable due to MUSCL reconstruction. For Test-1 with moderately relativistic conditions, MUSCL reconstruction was more effective in the reduction of L_1 error (approximately 68−71%) across all primitive variables. The strong relativistic case, Test-2, shows significant error reduction in velocity (80.9%) and pressure (68.6%), while density showed comparatively moderate improvement (35.3%). This is because velocity and pressure are more sensitive to steep gradients and strong discontinuities and hence benefit more from higher-order reconstruction, whereas density errors remain influenced by contact discontinuities.

The reduction in L_2 error is comparatively smaller, as it gives greater weight to localized large errors near discontinuities, which persist even with higher-order reconstruction. Similarly, there is even lower improvement in $L\infty$ norm, since it is governed by the maximum local error, typically occurring at shock and contact discontinuities. Pressure exhibits sharper gradients and larger magnitude jumps, leading to higher peak errors in first-order solutions, which are significantly reduced with MUSCL reconstruction (23.7% for Test-1 and 32.9% for Test-2). In contrast, velocity profiles are comparatively smoother, resulting in smaller initial peak errors and

consequently less pronounced improvement (1.2% for Test-1 and 0.3% for Test-2) in the $L\infty$ error norm.

Table 3: Percentage reduction in error norms achieved by MUSCL reconstruction relative to first-order scheme.

Tests	Error Norms	ρ (%)	v (%)	p (%)
Test-1	L_1	70.6	68.3	69.6
	L_2	45.3	43.7	56.9
	$L\infty$	1.9	1.2	23.7
Test-2	L_1	35.3	80.9	68.6
	L_2	6.5	59.6	54.7
	$L\infty$	13.33	0.3	32.9

While the HLLE scheme provided a stable and robust solution, MUSCL reconstruction, even though computationally complex and expensive, significantly improved the spatial accuracy and enhanced agreement with the benchmark solutions, even under strong relativistic conditions.

4.2 Numerical Sensitivity Analysis

4.2.1 Mesh Sensitivity

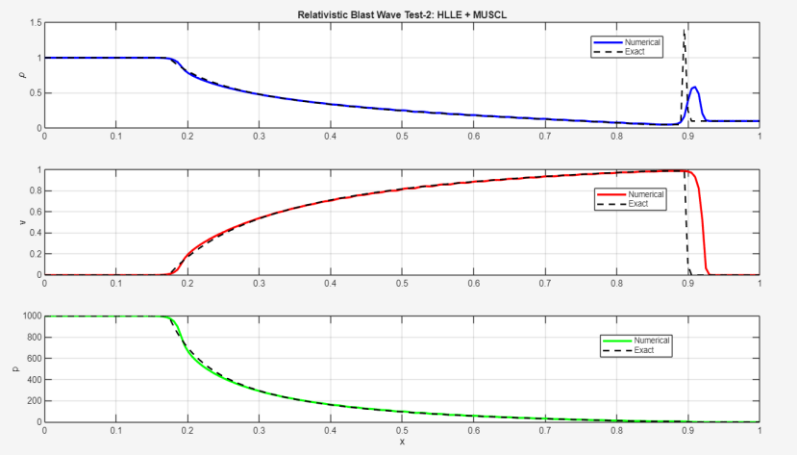

a) 200 cells

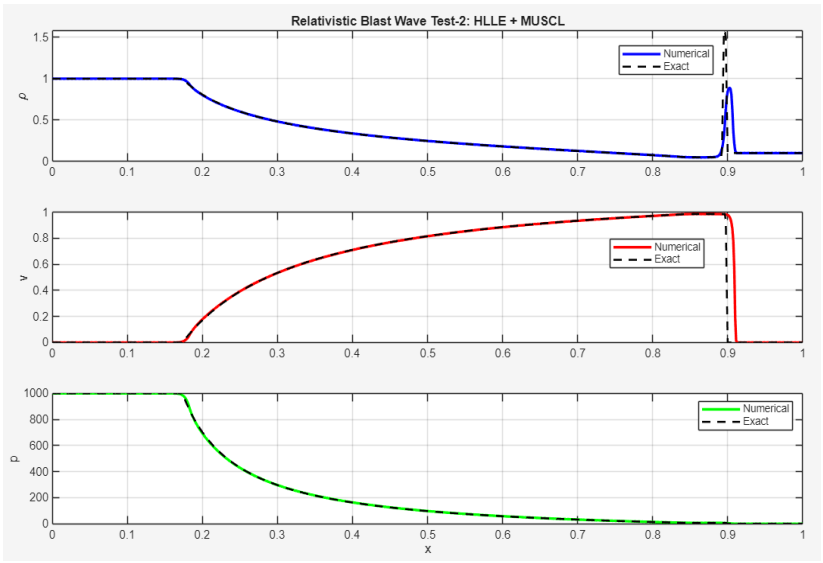

b) 800 cells

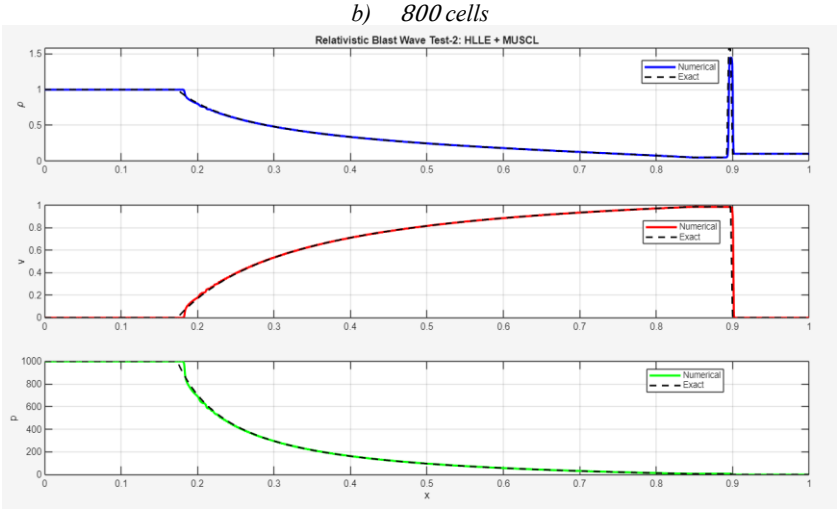

c) 2000 cells

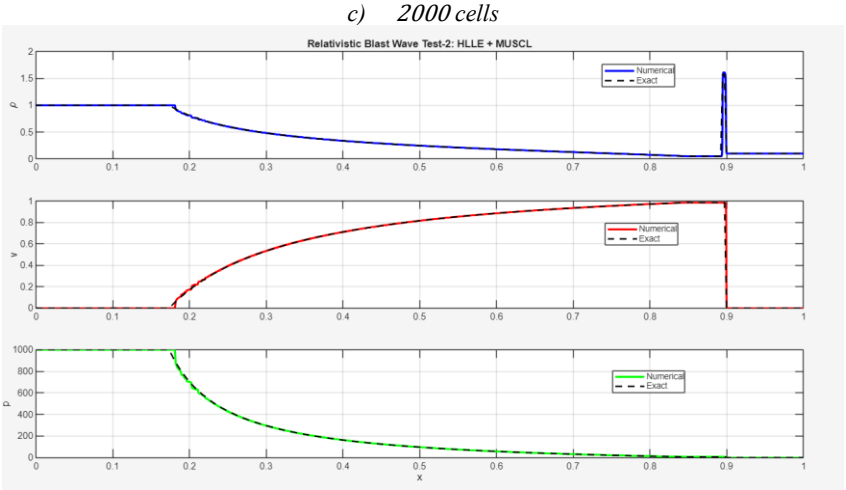

d) 4000 cells

Figure 6: Primitive variables profile analysis based on mesh sensitivity.

For the analysis of the effect of grid resolution on the numerical solution, four different sizes of mesh, 200 grids, 800 grids, 2000 grids and 4000 grids, were taken. All the plots, incorporating different cell numbers, were generated using the relativistic blast wave Test-2 under MUSCL reconstruction for better comparison. While the rarefaction region remains comparatively well captured even at lower resolutions, increasing resolution, as shown in Figure 6, sharpens the resolution discontinuities and reduces the numerical diffusion indicating better convergence of the numerical solution, particularly in the regions of strong gradients. The error norms presented in Table 4 show a consistent decrease in L_1 error with increasing grid resolution.

Table 4: Mesh convergence based on L_1 error norm for Test-2 under MUSCL reconstruction.

Cells	ρ	v	p
200	1.834e-02	2.482e-02	3.763e+00
800	1.098e-02	7.888e-03	2.795e+00
2000	5.775e-03	3.590e-03	1.806e+00
4000	3.541e-03	1.976e-03	1.283e+00

The L_1 error in density was reduced by over 80% while increasing cells from 200 to 4000, while the velocity error decreased more significantly (approximately 92%) over the increased grids. A similar trend can be observed for pressure, where the error decreased from 3.763 to 1.283. The comparatively slower decrease in pressure error (around 65%) can be attributed to the presence of strong discontinuities. Higher the number of cells in defined domain, greater the agreement with exact solution, however it also increases computational cost. Based on this observation, a suitable grid resolution that provides balance between numerical accuracy and computational efficiency can be selected.

4.2.2 CFL Number

Simulations on relativistic blast wave Test-2 using MUSCL reconstruction were performed for different CFL numbers that showed the stability limit for this test case is a Courant number of approximately 0.65. Any higher CFL number than that brought in numerical error thus terminating the simulation. The effect of CFL number in numerical solutions can be analyzed through Figure 7 which shows primitive variables profiles for CFL numbers of 0.1, 0.3, 0.5 and 0.65, respectively.

The study clearly depicts that the CFL condition controls the size of the time step thus affecting stability and temporal accuracy, with a relatively small impact on shock resolution. For this test case, a lower CFL value of 0.1 resulted in stable and smoother solutions, while higher values like 0.65 produced noticeable oscillations and reduced stability. Lower CFL, however, made the simulation slower due to the increase in the number of iterations caused by smaller time steps, while simulations were faster with the increasing value of CFL number. Larger time step errors were introduced by higher CFL values while lower values of CFL increased the computational cost. The moderate CFL values (0.3–0.5) yielded minimal oscillations and numerical diffusion hence providing a balance between stability and computational efficiency.

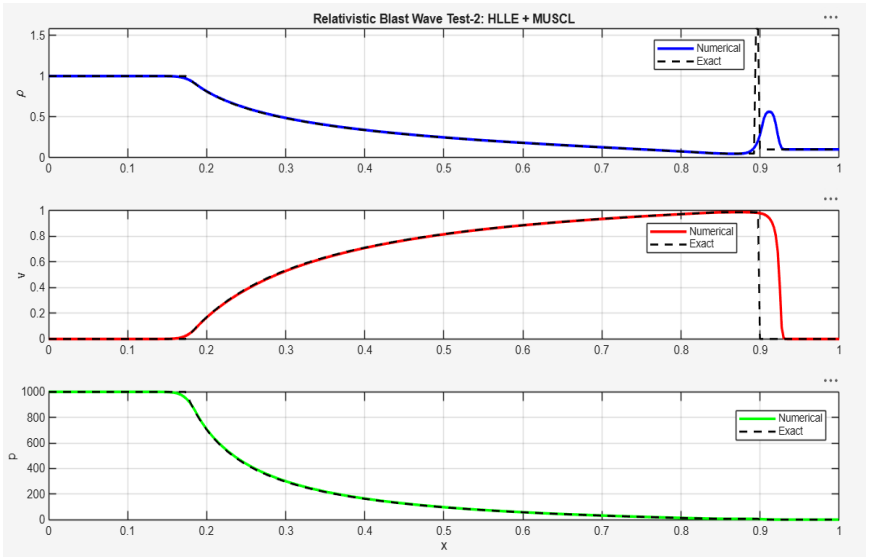

a) CFL = 0.1

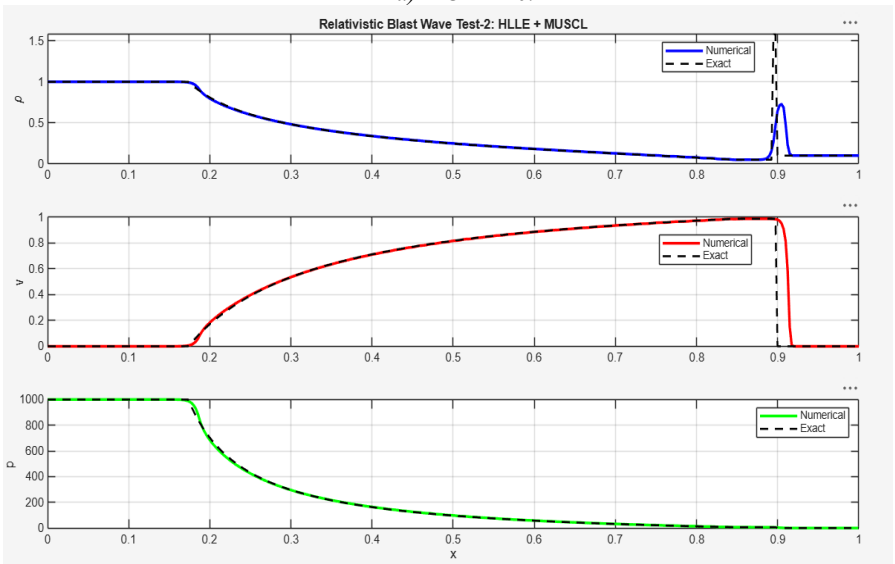

b) CFL = 0.3

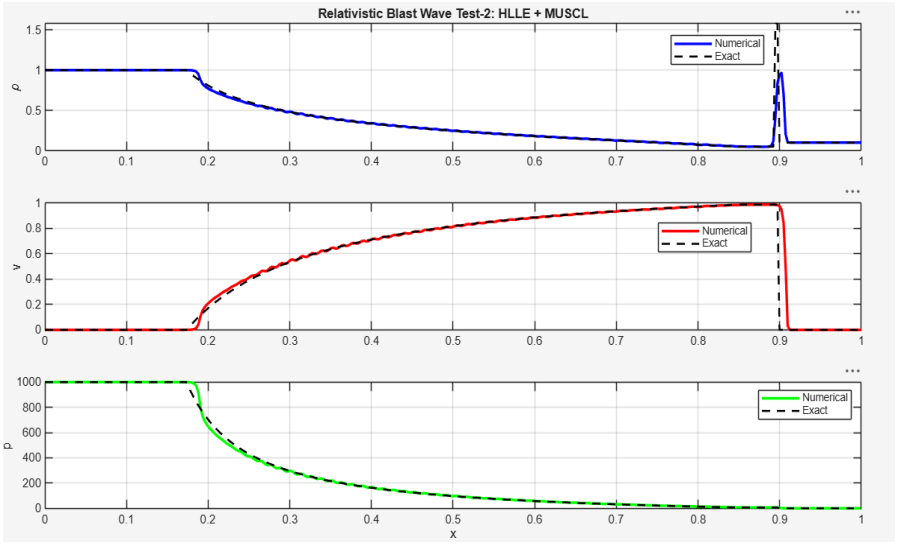

c) CFL = 0.5

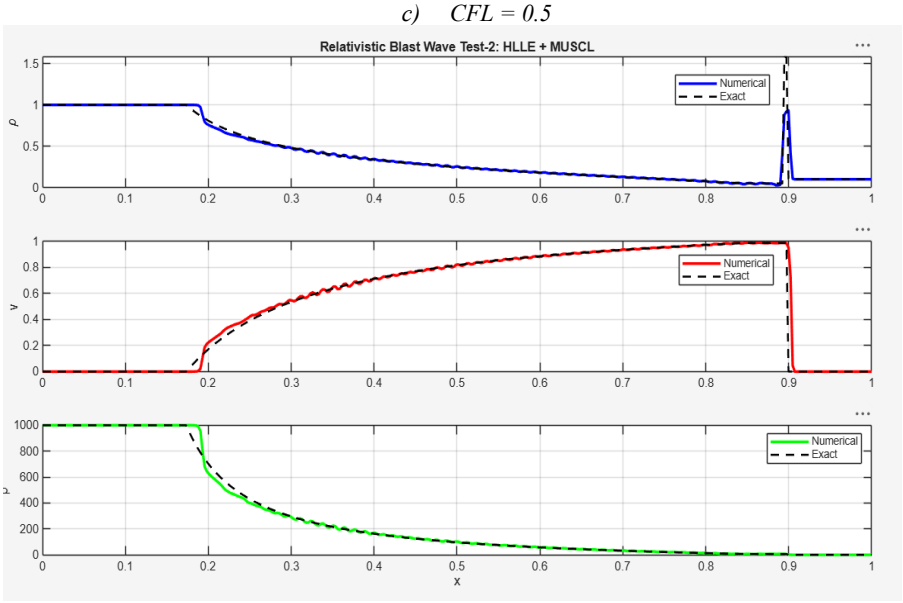

d) CFL = 0.65

Figure 7: Primitive variable profiles at different Courant numbers.

The effect of CFL number on solution accuracy was further evaluated with the analysis of L_1 error norms for primitive variables and presented in Table 5. As the Courant number was increased from 0.1 to 0.65, the error in density decreased by approximately 23.8% and velocity error decreased by approximately 56.8%. The reduction in numerical diffusion here is due to smaller time steps and a larger number of iterations resulting from a higher CFL number. But for pressure error which increased significantly by approximately 302%, the increase is due to increased time discretization error and sensitivity of pressure to larger time steps near the stability limit.

Table 5: L_1 error norms for different CFL numbers (Test-2, MUSCL).

CFL	ρ	v	p
0.1	1.825e-02	2.570e-02	1.930e+00
0.3	1.568e-02	1.521e-02	2.795e+00
0.5	1.551e-02	1.285e-02	5.089e+00
0.65	1.391e-02	1.111e-02	7.337e+00

Unlike grid refinement, variation in CFL number does not substantially sharpen discontinuities. This is because numerical diffusion in finite-volume schemes is primarily governed by spatial discretization and reconstruction methods rather than time step size. Even though CFL affects stability and efficiency, its role in improving solution accuracy is secondary compared to mesh refinement.

4.3 2D SRHD Solver Validation

The validated 1D SRHD solver was extended to a two-dimensional computational domain by imposing the initial conditions from 1D relativistic blast wave Test-1 uniformly in the transverse (y) direction, resulting in a planar shock configuration that is invariant along y. Grid size for this case was set as 200 cells each in both directions resulting in a matrix of 40,000 elements. Two boundary layers were added to each of the four sides of the rectangular domain of non-dimensionalized length [0, 1] for both directions. Following the earlier results on the benefits of second order spatial reconstruction, MUSCL scheme with slope limiting was used in combination with the HLLE Riemann solver.

4.3.1 Primitive Variable Fields and Wave Structure

Figure 7 presents the 2D field visualization of the recovered primitive variables at final time, t = 0.4. The 1D Riemann wave structure is uniformly extended in transverse direction. The solution consists of high density and pressure to the left followed by a rarefaction wave, which smoothly transitions to contact discontinuity terminated by the right moving shock wave that low density and pressure region toward the right. Driven by the strong pressure gradient, the variables vary smoothly within rarefaction region. The contact discontinuity that follows, is identified by a sharp jump in density while pressure and velocity remain continuous across it. The sharp discontinuity

at $x \approx 0.8$ in all primitive variables captures shock wave confirming the correct compressive wave behavior in numerical solution of 2D SRHD quite identical to that of 1D SRHD solver.

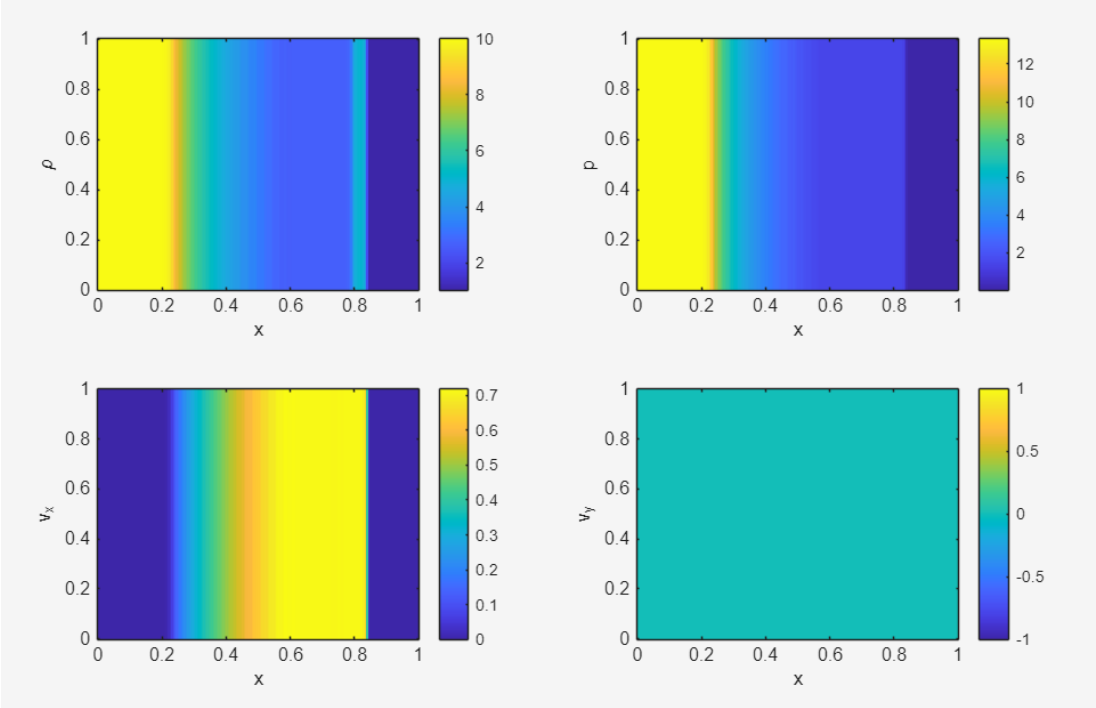

Figure 8: Primitive variables 2D filed visualization

With $v_\gamma = 0$ everywhere, the velocity field exhibits smooth acceleration through the rarefaction fan which confirms that the extension to 2D preserves the symmetry and introduces no transverse numerical errors.

4.3.2 Centerline Primitive Variables Profiles (1D Slice)

Analogous to the 2D field visualization from Figure 7, the 1D slice of the centerline profiles also exhibit consistent behaviour of rarefaction, contact discontinuity, and shock wave. Figure 8 demonstrates a good agreement of 2D solver's solution with the reference solution indicating towards solver's accuracy and its dimensional consistency thereby confirming its validation against benchmark test problem.

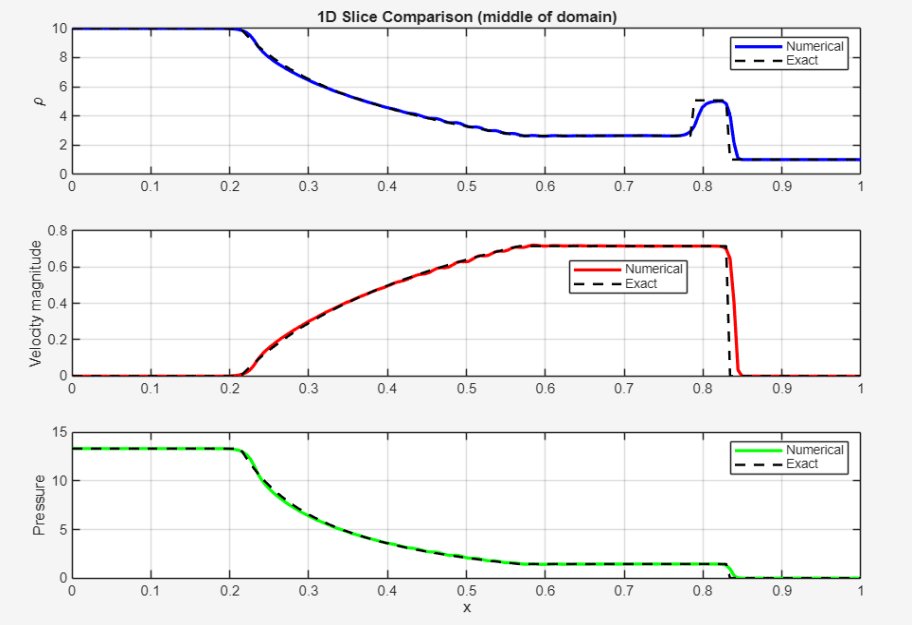

Figure 9: Centerline (1D slice) primitive variable profiles extracted from the 2D SRHD solution

The error norms for density, velocity and pressure in Table 2, are comparatively higher than that for 1D solution of same test case. The elevation of errors is resulted by increase in computational cells involved in 2D. Further, the presence of sharp discontinuities and increased numerical diffusion increase the errors while still maintaining correct wave structure.

Table 6: Error norms of respective primitive variables for relativistic blast wave Test-1 simulated in 2D SRHD solver.

Error norms	**Density (ρ)**	**Velocity (v)**	**Pressure (p)**
L_1	3.634e+00	3.455e-01	5.377e+00
L_2	4.621e+00	4.449e-01	7.195e+00
$L\infty$	9.000e+00	7.194e-01	1.333e+01

4.4 2D SRHD Circular Blast Wave Simulation

For the circular blast wave simulation 400 physical cells in both direction along with 2 layers of ghost cells as boundary were set in all four sides of the computational domain of size [0, 1] in both x and y direction. Initial conditions for this simulation were defined as purely pressure-driven explosion with no initial bulk motion. The velocity field was set to zero at t=0, throughout the domain. A high-pressure, high-density region with $\rho = 10$ and $p = 13.33$, was prescribed inside a circular region of radius $R = 0.1$ with center at $(x_0, y_0) = (0.5, 0.5)$, while the surrounding ambient medium was assigned $\rho = 1$ and $p = 10^{-6}$. Unlike in simulation for solver validation against benchmark tests, in this simulation adiabatic index (Γ) = 4/3 was used to ensure that the internal energy becomes comparable to the rest-mass energy in the post-shock region, leading to a locally relativistic flow behavior. The computation is run for final time t = 2.

4.4.1 Spatial Distribution of Primitive variables

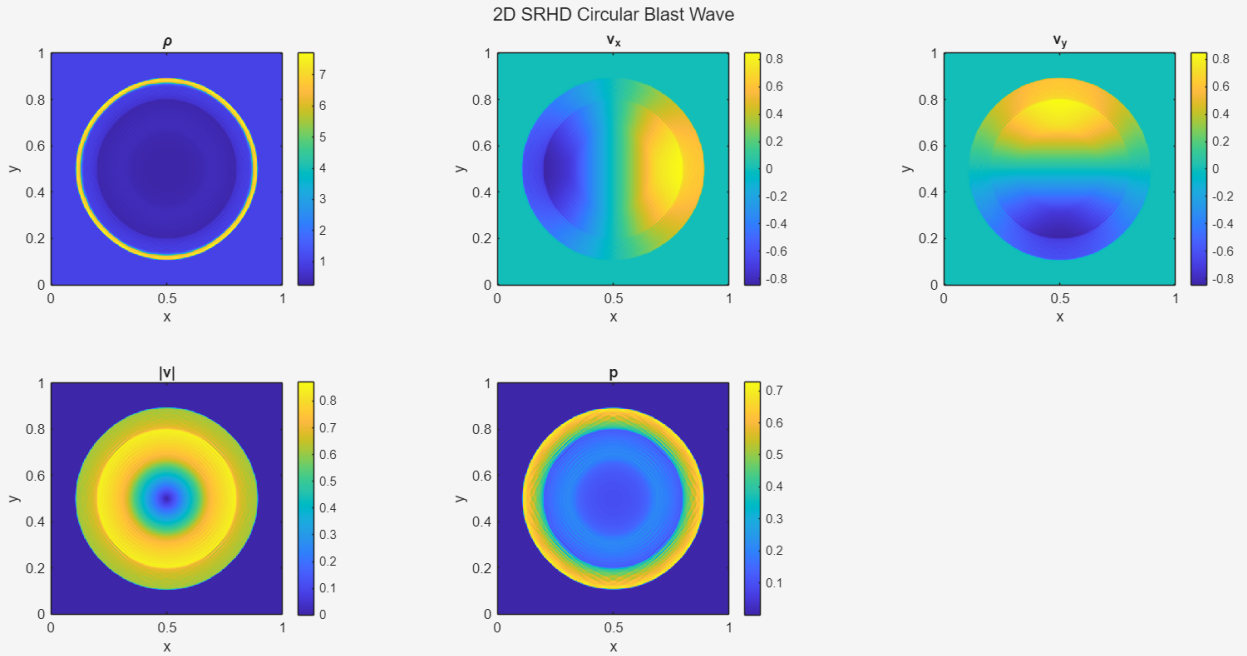

Figure 100: 2D field visualization of primitive variables for circular blast wave

A radially symmetric two-dimensional contour plots of primitive variables for circular blast wave is presented by Figure 10. It shows that the solution originates from the center of the domain of

localized high-pressure region and the flow expands towards the low-pressure and low-density ambient surrounding due to strong pressure ratio of order $10^{7.}$

As the fluid is pushed outward, fluid expands radially and the mass is transported away from the center. This results in the decrease in density therefore creating a low-density core which is surrounded by a thin high-density ring corresponding to contact discontinuity and an outer ring of shock front. Beyond the shock, density matches the ambient state and remains uniform.

The velocity components v_x and v_y, starting from rest at the center, undergo directional sign change along their coordinate axes exhibiting antisymmetric pattern. A slight diffusion can be observed in the velocity components near center due to the absence of a well-defined radial direction at r = 0 on which they depend. In contrast, the velocity magnitude remains well defined, increasing radially from zero at the center. It forms a high-velocity shell reaching approximately to 0.8 indicating relativistic behavior. The velocity later drops to zero beyond the shock front.

The central high pressure decreases throughout the rarefaction zone incorporating expansion. As it can be seen in Figure 10, the decrease in pressure appears almost uniform until the shock front due to extremely low ambient pressure. The field visualization shows stable shock capturing due to absence of oscillations near discontinuities.

The overall field presents a radially expanding relativistic blast wave structure consisting of a rarefaction region, a contact discontinuity, and an outward propagating shock.

4.4.2 Radial Symmetry Verification

The radial symmetry observed in field visualization from Figure 10 was further confirmed by plotting primitive variables against radial distance. Figure 11 demonstrates, clearly, that the solution for circular blast wave solely depends on radial distance. All the data collapsing into a well-defined profile indicates that the radial symmetry is preserved.

As the rarefaction moves inward, center no longer consists of high density and pressure resulting the pattern as shown by Figure 11. As described in previous section, velocity components depict antisymmetric pattern across the domain visible in the figure below, while the velocity magnitude remains symmetric.

Just like the field visualization, radial profile also captured the key flow features, including the variation across the rarefaction region and the sharp transitions associated with the contact discontinuity and shock front.

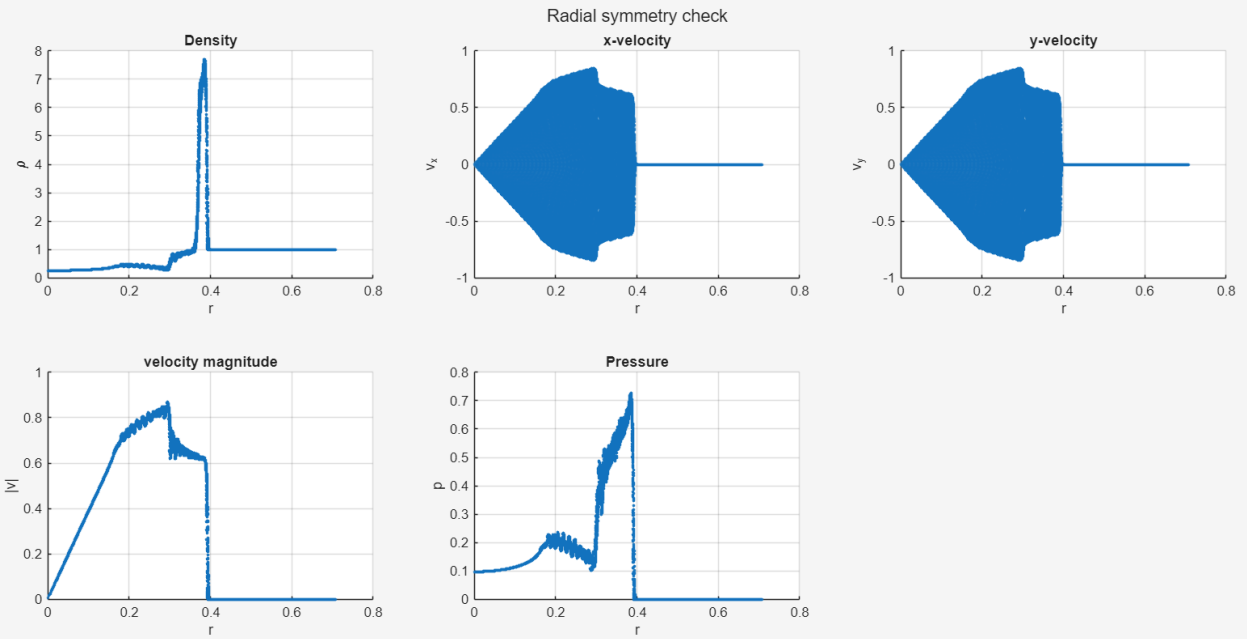

Figure 11: Primitive variables evolution over radial distance.

4.5 Relativistic Jet Propagation Simulation

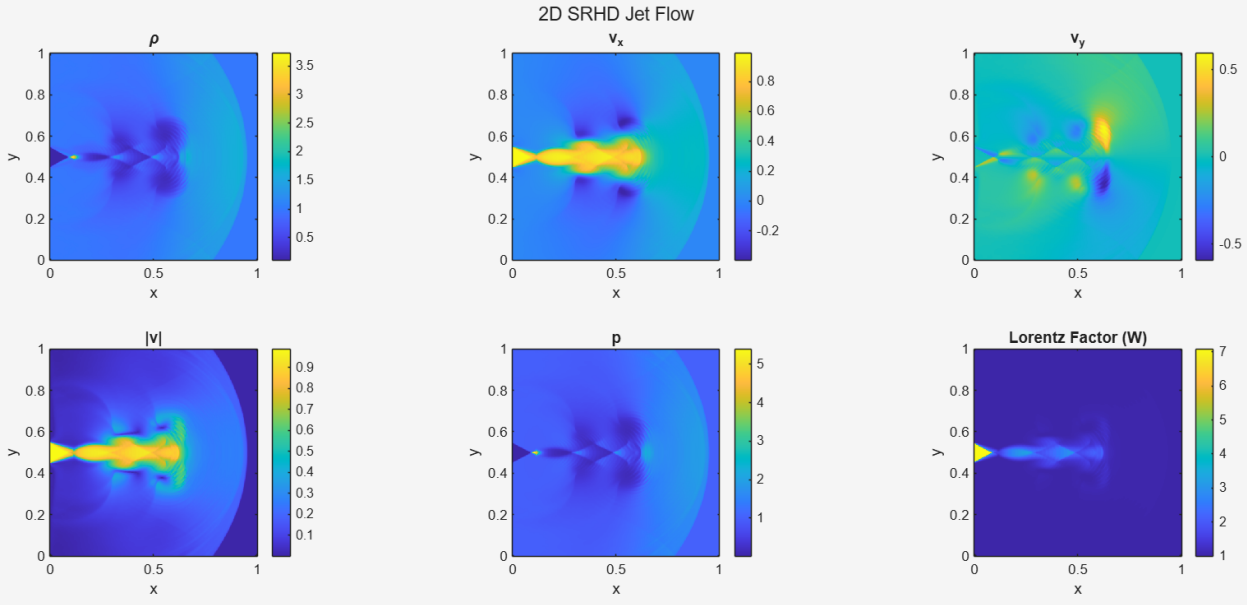

Figure 12: Field visualization of relativistic jet.

The jet propagation simulation was run on a two-dimensional computational domain [0,1] × [0,1] discretized using 400 × 400 grid cells with two layers of ghost cells on each boundary. A relativistic jet was injected from the left boundary ($x = 0$) into a uniform ambient medium. Initially, the domain was filled with ambient conditions $\rho = 1$, $v_x = 0$, $v_y = 0$, $p = 1$. For $t \geq 0$, a jet inflow condition was imposed within a radius of 0.05 centered at $y = 0.5$, defined by $\rho = 0.1$, $v_x = 0.99$, $v_y = 0$, $p = 0.01$, while the remaining inlet region retained ambient conditions. This introduces a strong discontinuity in density, pressure, and velocity at the inlet. The adiabatic index $\Gamma = 4/3$ is used to represent relativistic flow while the flow evolves under a MUSCL–HLLE finite volume scheme.

The field visualization of primitive variables and Lorentz factor in Figure 12 shows the development of a typical relativistic jet morphology. Near the inlet a narrow, high-speed, low-density jet core propagates along the x-direction, forming a well-collimated beam. As the jet interacts with the dense ambient medium, a bow shock forms ahead of the jet head, which is visible as a curved high-pressure and high-density region. This structure arises due to the relativistic impact of the jet on the stationary medium, where the bulk kinetic energy is converted into thermal energy through strong compression. The flow exhibits a complex internal structure characterized by alternating compression and expansion regions. These appear as diamond-shaped patterns along the jet axis and correspond to internal (recollimation) shocks, which develop due to pressure difference between the jet and the surrounding medium as the jet moves toward pressure balance. The jet continuously adjusts its cross-section through these compression–expansion cycles as it propagates downstream.

The contrast between the light jet core and the dense ambient medium is clearly visible in density field. Near the inlet, the jet spine is relatively collimated but as the jet propagates downstream it is gradually distorted due to entrainment and mixing with the ambient fluid. The compressible nature of the flow is captured by pressure field. There are strong localized peaks at the bow shock and internal shock locations, and smoother variations in expansion regions associated with rarefaction waves. These rarefaction regions are characterized by gradual decreases in pressure and density, in contrast to the sharp gradients observed at shock fronts. A contact discontinuity is present between shocked jet and shocked ambient medium. Even though, it is not sharply visible in the results due to the diffusive nature of the HLLE solver, which tends to smear such interfaces, the overall flow structure is preserved.

The axial velocity v_x remains close to relativistic values near the inlet as the jet maintains a strong forward momentum along the centerline. The flow progresses with a decrease in v_x in the regions affected by shocks and mixing for the momentum is transferred to the ambient medium. The transverse velocity v_x, initially zero, develops non-zero values along the jet boundary due to lateral expansion induced by transverse pressure gradients and shear at the contact region, leading to a subsequent mixing with the ambient medium. The purely axial flow transitions into a two-dimensional structure with significant cross-stream motion. The velocity magnitude displays a gradual deceleration and spreading of the jet as it propagates downstream.

A shear layer forms due to the large velocity gradient at the interface between the high-speed jet and the stationary ambient medium. This shear layer becomes unstable and gives rise to Kelvin–Helmholtz instability, which is observed as wavy distortions and vortical structures along the jet boundary, particularly in the transverse velocity field. The jet expands in y-direction hence losing the sharply defined boundary due to the mixing between the jet and ambient fluid caused by the instabilities. Similarly, the Lorentz factor distribution shows high values concentrated along the jet core where the flow remains relativistic, and reduced values in shocked and mixed regions where the flow decelerates.

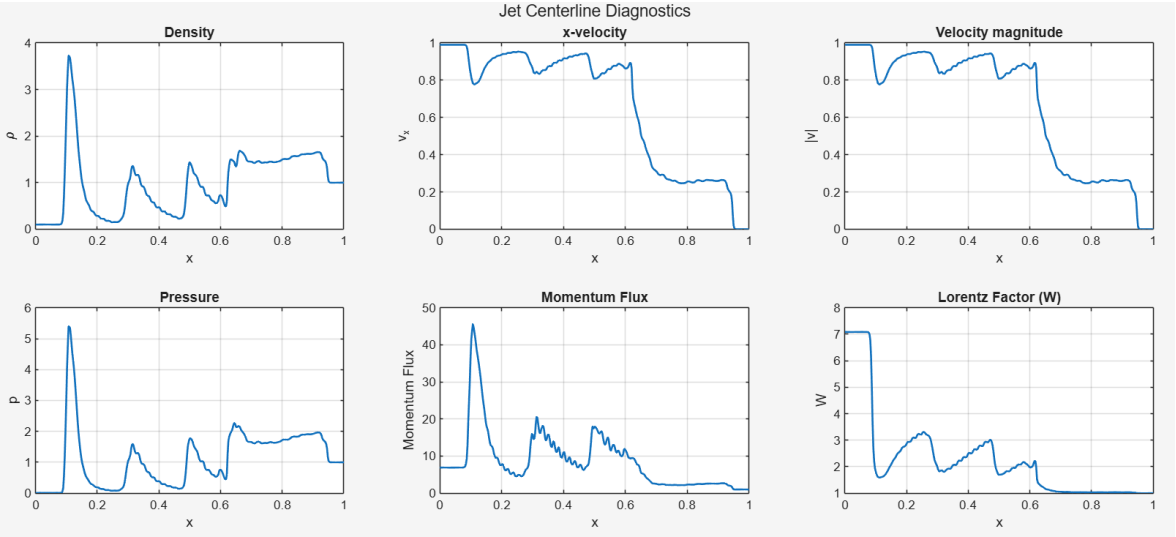

Figure 13: Jet centerline diagnostics

The centerline diagnostics shown in Figure 13, extracted along $y = 0.5$, provide a quantitative one-dimensional representation of the jet evolution. The density profile shows the persistence of the low-density jet core and its gradual modification due to interaction with the ambient medium. The axial velocity profile shows that the jet retains a high-speed core over a considerable distance, over approximately $x = 0.4$, after which it gradually slows down downstream, from $v_x = 0.99$ to nearly 0.7 downstream due to shock interactions and the transfer of momentum to the surrounding medium. The regions of compression associated with shock structures can be seen in pressure profile where the smoother variations represent expansion zones linked to rarefaction waves. The Lorentz factor profile displays the highly relativistic jet core ($W \approx 7$) which gradually decays downstream. In a similar way, the momentum flux also declines by around 90% along the flow direction due to mixing and energy dissipation.

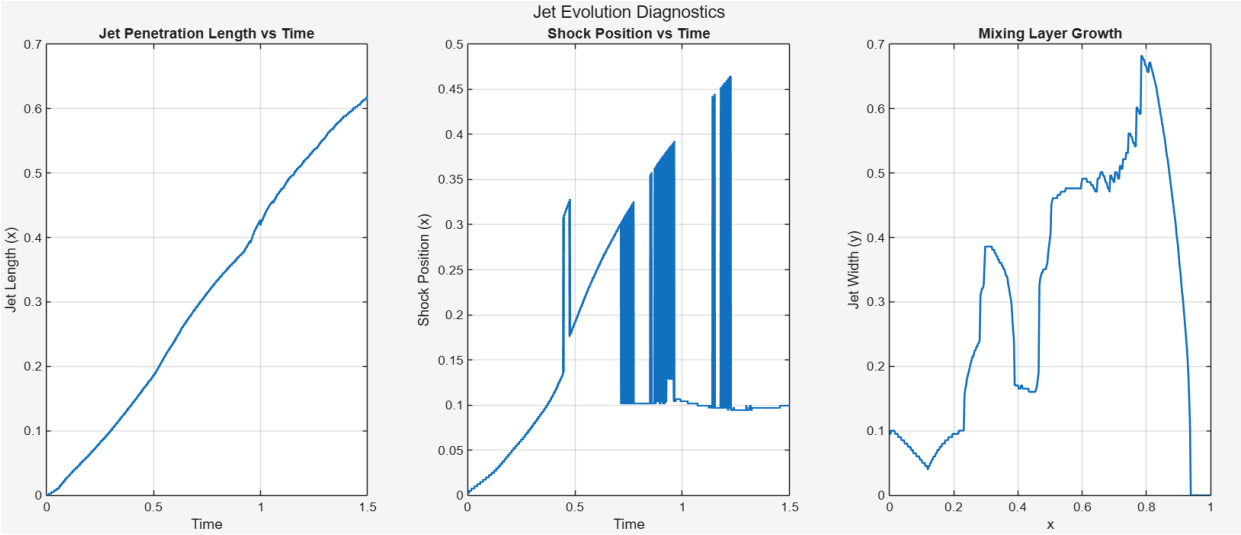

Figure 14: Jet evolution diagnostics.

The jet evolution diagnostics in Figure 14 further quantify the global behavior of the flow. There is a sustained propagation of the jet into the ambient medium as jet penetration length increases almost linearly with time. A dynamic interaction between the jet and its surroundings can be seen in shock position vs time plot which tracks the movement of the bow shock, determined from the maximum pressure gradient along the centerline. The mixing layer width, computed based on a velocity threshold (0.2), increases along x-axis, providing clear quantitative evidence of shear-

driven instability growth. This growth is directly associated with Kelvin–Helmholtz instability and indicates progressive entrainment of ambient fluid into the jet.

4.5.1 Effect of Lorentz Factor on Jet Dynamics

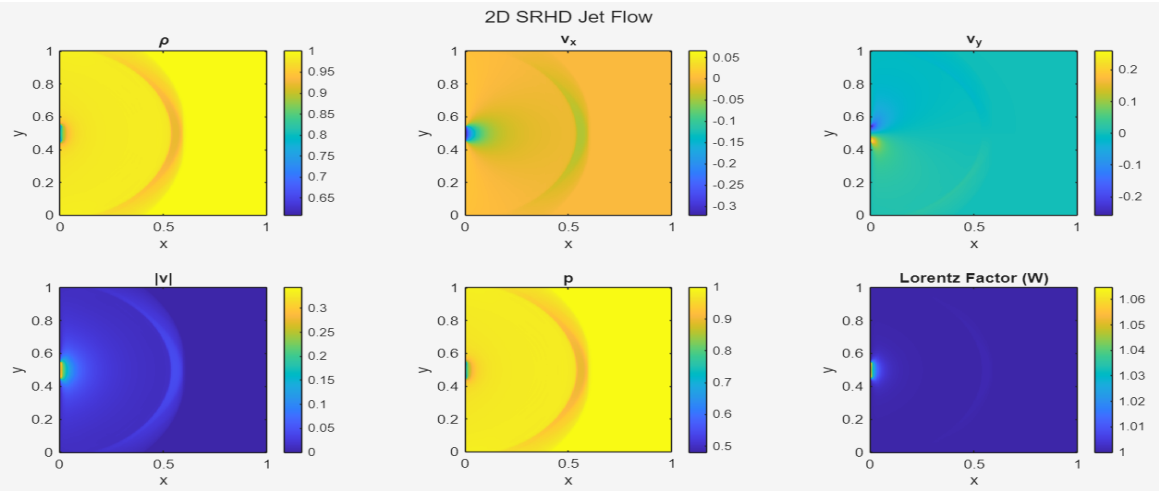

a) $W \approx 1.67$

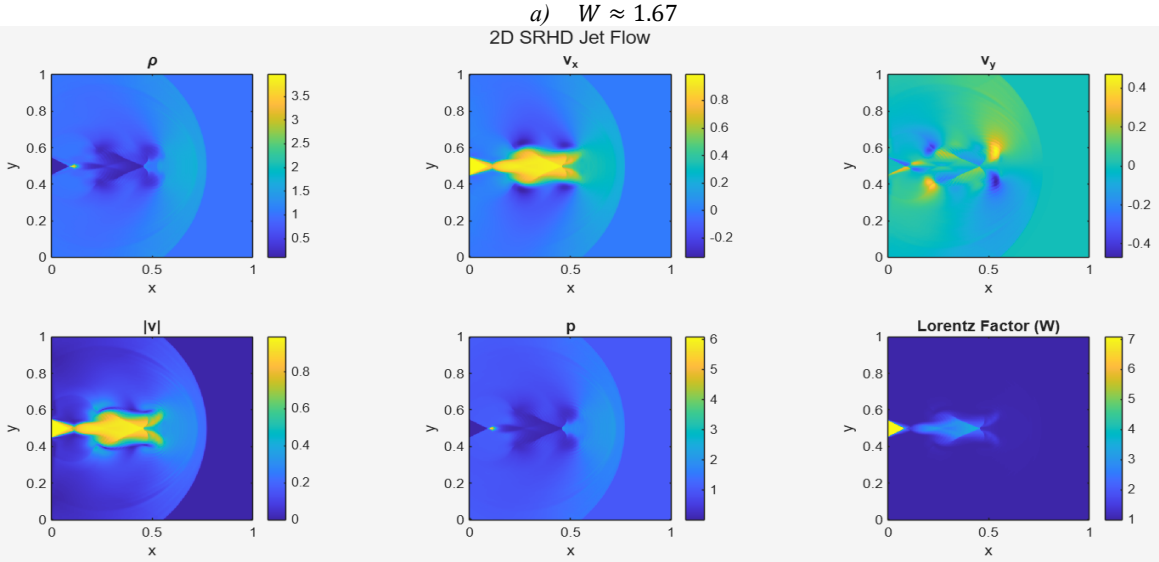

b) $W \approx 7.09$

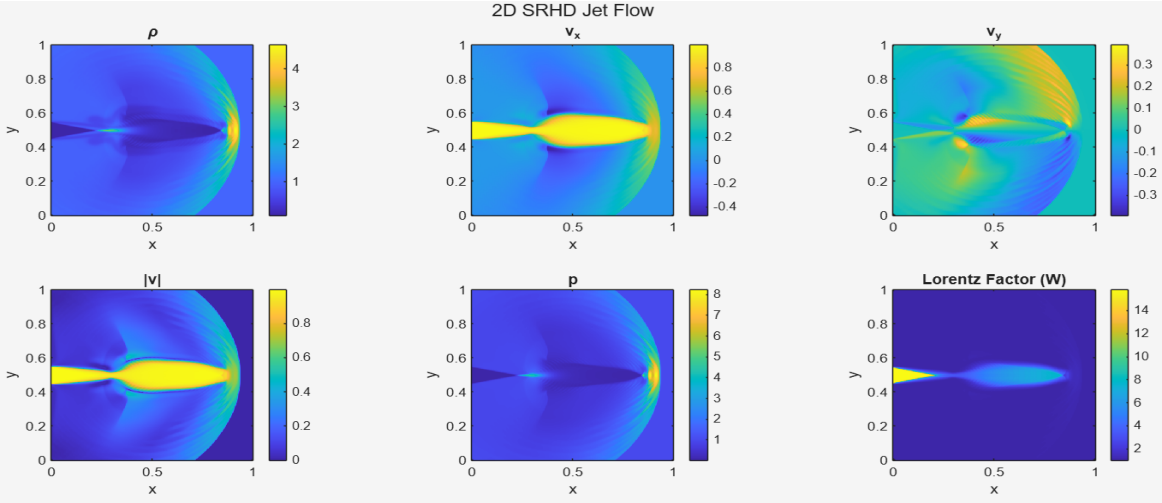

c) $W \approx 15.81$

Figure 15: 2D field visualization of Lorentz Factor effect on jet dynamics.

For analyzing the effects of Lorentz factor on jet dynamics, three injection velocities were considered, $v_x = 0.8$, 0.99, and 0.998, corresponding to Lorentz factors $W \approx 1.67$, 7.09, and 15.81. The relativistic jet was injected from the left boundary ($x = 0$) into the uniform ambient medium with a strong density and pressure contrast ($\rho_j = 0.1$, $p_j = 0.01$ for the jet and $\rho_a = 1$, $p_a = 1$ for the ambient). The jet is purely axial at injection ($v_y = 0$) and confined within a radius $r_j = 0.05$ centered at $y = 0.5$. The computational domain $[0,1] \times [0,1]$ is resolved with a 400×400 grid, evolved to $t = 1.2$ using a CFL number of 0.4 and an adiabatic index $\Gamma = 4/3$. Since all other parameters remain fixed, the differences in jet evolution directly reflect the role of relativistic inertia and momentum flux. The global flow structures for these cases are illustrated in Figure 15, while centerline and evolution diagnostics are shown in Figures 16 and 17, respectively.

At the lowest Lorentz factor, $W \approx 1.67$, the jet rapidly loses coherence shortly after injection, as seen in the density and velocity fields in Figure 15(a). Initially the jet core is under-dense but within a short downstream distance ($x \sim 0.2$) it gets strongly contaminated by ambient material, and the density increases toward $\rho \sim 0.9$. The injection value $v_x = 0.8$ of the axial velocity decreases to approximately 0.3, while transverse velocities grow to about $v_y \sim \pm 0.2$, with pronounced lateral spreading. The jet width increases from the initial 0.05 to approximately 0.25–0.30, as seen in the mixing-layer diagnostic in Figure 17(a). The flow exhibits Kelvin–Helmholtz (KH) instability, with strong distortions along the shear layer and intense interaction

between the jet and ambient medium. Relativistic features are rapidly lost as the Lorentz factor decreases toward $W \approx 1$. The bow shock forms at the jet head, but remains relatively close to the inlet ($x \sim 0.25$–0.35) due to limited penetration. It appears broader and weaker compared to higher Lorentz factor cases. The jet in this regime is dominated by instability-driven mixing and rapid momentum dissipation.

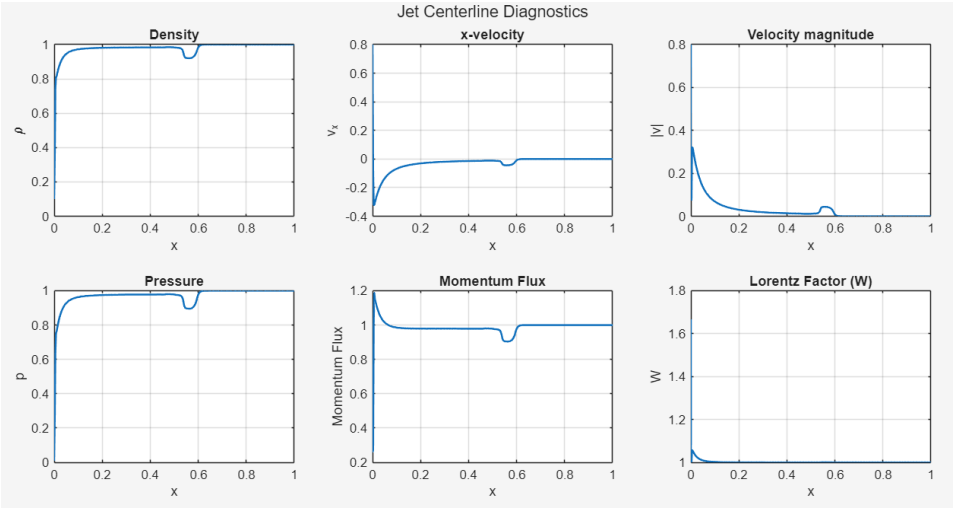

a) $W \approx 1.67$

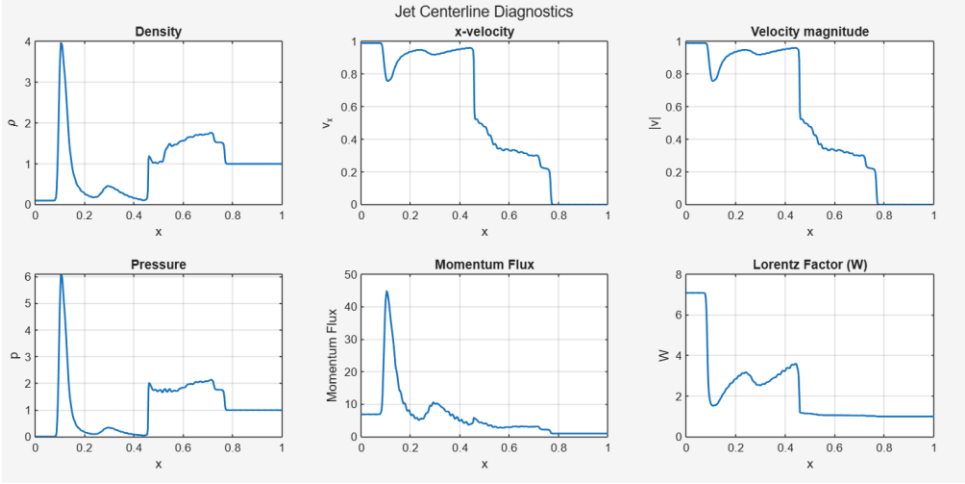

b) $W \approx 7.09$

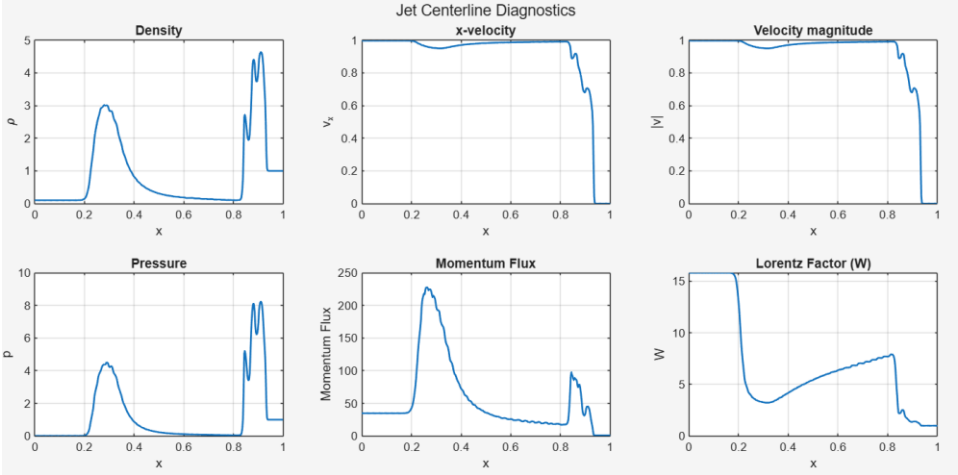

c) $W \approx 15.81$

Figure 16: Centerline profiles illustrating the effect of Lorentz factor on jet dynamics.

For the intermediate Lorentz factor ($W \approx 7.09$), the jet exhibits increased collimation and stability, as shown in Figure 15(b). The jet penetrates further into the domain, reaching approximately $x \sim 0.5$. It develops a clearer internal structure that consists of a relatively intact core and a surrounding shear layer. The density field shows that the core remains under-dense with $\rho \sim 0.4$. The axial velocity remains high ($v_x \sim 0.8$) over a significant downstream distance, while transverse velocities are reduced to approximately $v_y \sim \pm 0.15$. The centerline profiles in Figure 16(b) are consistent with these behaviours where both velocity and Lorentz factor decay more gradually. Even though the Kelvin–Helmholtz instability is still present, its growth is slower and largely confined to the outer shear layer, without significantly disrupting the jet core. The bow shock is stronger and shifted downstream to approximately $x \sim 0.55$. The pressure level is increased indicating stronger compression. The jet evolution plots in Figure 17(b) confirm this behavior, with increased penetration length and reduced mixing with ambient medium compared to the low-W case. This regime represents a transitional state in which relativistic effects begin to suppress instability growth and enhance axial momentum transport.

In the highly relativistic case ($W \approx 15.81$), the jet remains strongly collimated and propagates across most of the computational domain, as clearly seen in Figure 15(c). The jet head reaches approximately $x \sim 0.9$. The density field maintains a sharp interface between the jet core ($\rho \sim 0.3$) and the ambient medium, indicating minimal mixing. While the transverse velocities are

strongly suppressed ($v_y < 0.05$), the axial velocity remains nearly constant. The Lorentz factor remains high ($W \sim 10$–15) along most of the jet spine, with sustained relativistic motion. In this regime, Kelvin–Helmholtz instability is significantly suppressed, with the shear layer remaining thin. The bow shock is sharply defined and located far downstream ($x \sim 0.95$), with higher peak pressure compared to lower-W cases, indicating strong compression at the jet head. The jet evolution diagnostics in Figure 17(c) shows characteristic of a stable, high-momentum flow with a nearly linear increase in jet penetration length and a consistently narrow mixing layer,.

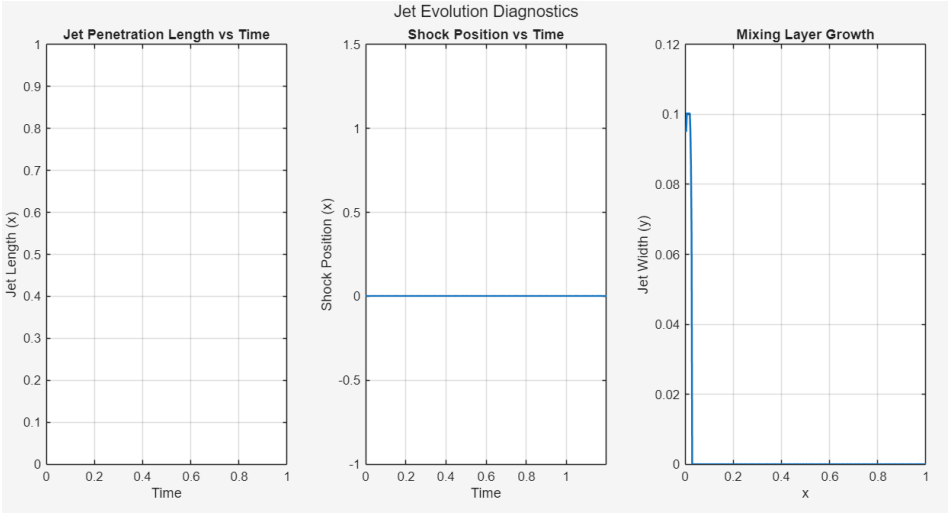

a) $W \approx 1.67$

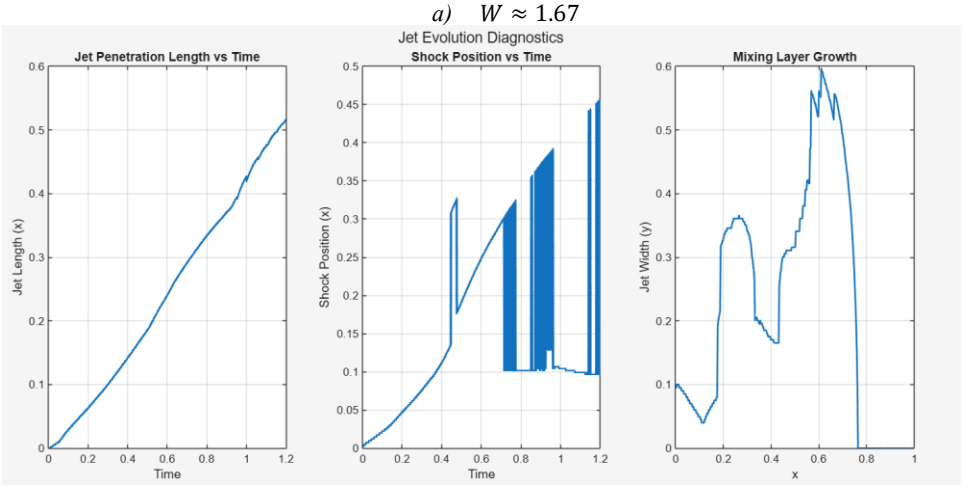

b) $W \approx 7.09$

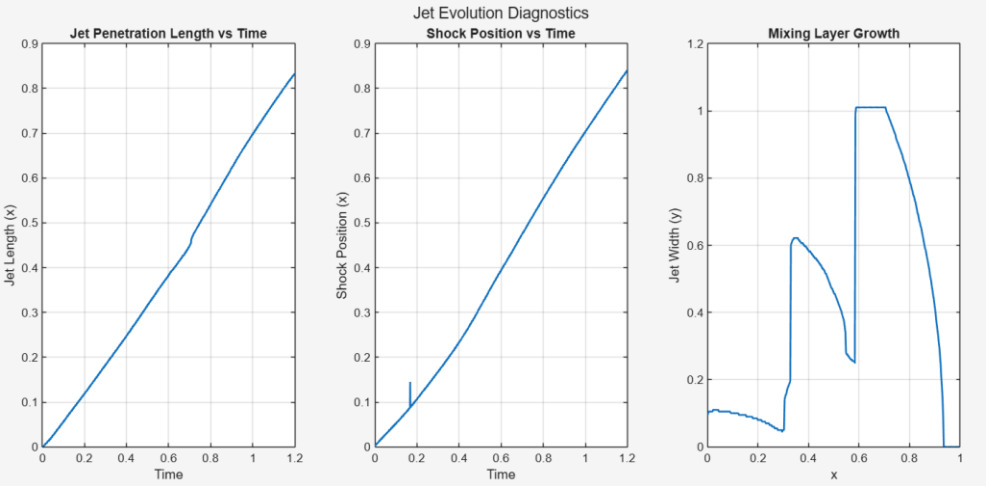

c) $W \approx 15.81$

Figure 17: Jet evolution diagnostics showing effect of Lorentz factor on jet dynamics.

The centerline and evolution diagnostics (Figures 16 and 17) provide a quantitative comparison across the three cases. The jet penetration length increases from approximately $L_j \sim 0.3$ in the low-W case to $L_j \sim 0.55$ and $L_j \sim 0.9$ for intermediate and high Lorentz factors, respectively. The bow shock position shifts downstream accordingly. The mixing layer growth plot shows that with the increase in Lorentz factor it takes more length of the domain for the jet to mix with the ambient medium. This is due to the reduction in mixing layer growth, indicating reduced entrainment with increasing W. The centerline Lorentz factor profiles show rapid decay in the low-W case, moderate decay in the intermediate case, and sustained high values in the high-W case.

The results demonstrate a clear transition in jet dynamics with increasing Lorentz factor. The jet is dominated by Kelvin–Helmholtz instability and turbulent mixing at lower Lorentz factor, leading to rapid loss of coherence. The instability growth is partially suppressed at intermediate W, allowing a stable persistence of the core alongside a moderate shear layer. And at high W, the flow is highly stabilized due to the large relativistic inertia $\rho h W^2$ that suppresses transverse motion, resulting in a highly collimated jet with strong axial momentum and minimal mixing. Overall, Lorentz factor plays a fundamental role in controlling jet stability, mixing, and propagation.

4.5.2 Effect of Density Contrast on Jet Dynamics

The relativistic jet is injected from the left boundary ($x = 0$) into a uniform ambient medium with fixed pressure and velocity conditions $(p_j = 0.01,\ v_x = 0.99,\ v_y = 0 \text{and}\ \rho_a = 1,\ p_a = 1)$. Three density ratios are considered by varying the jet density as $\rho_j = 0.01,\ 0.1,\ 0.5$, corresponding to density contrasts $\eta = \rho_j/\rho_a = 0.01,\ 0.1,\ 0.5$. All three simulations are run for final time, $t = 1.3$. The computational setup, numerical scheme, and all other parameters are kept unchanged, so as to link the observed differences in jet structure directly to the density contrast. The resulting flow fields are shown in Figure 18, while Figures 19 and 20 present the corresponding centerline profiles and jet evolution diagnostic, respectively.

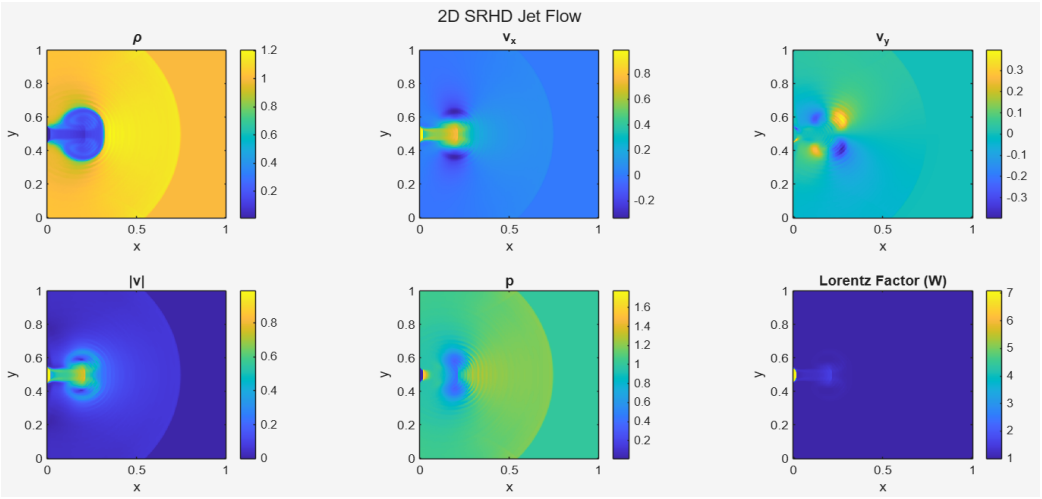

a) $\eta = 0.01$

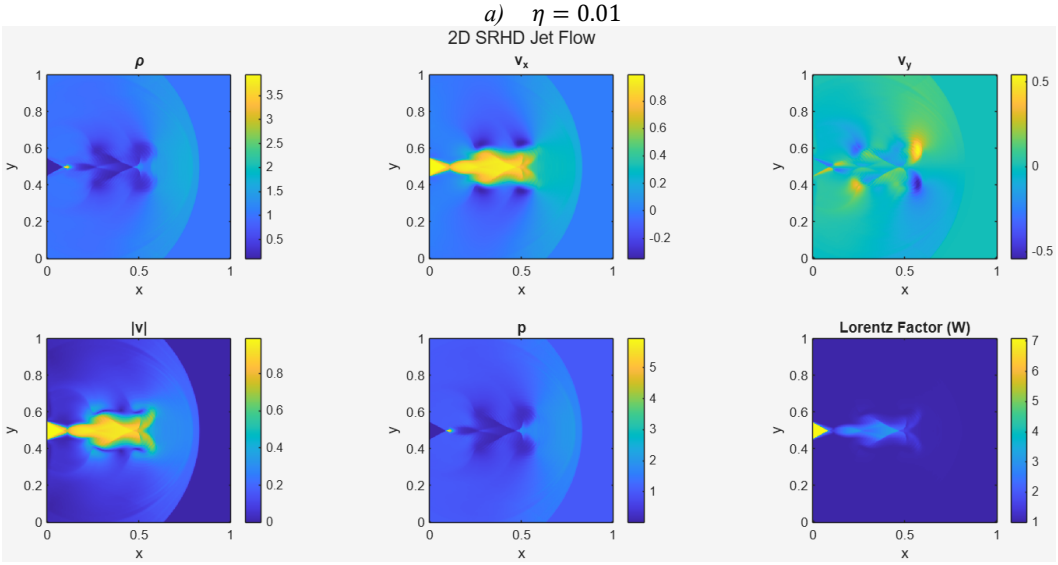

b) $\eta = 0.1$

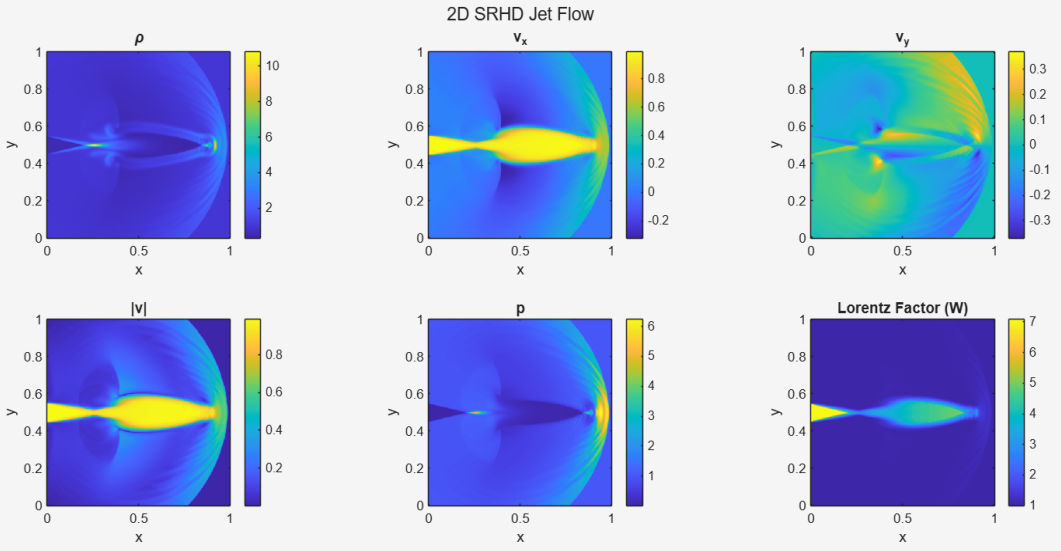

c) $\eta = 0.5$

Figure 18: Effect of density contrast on jet dynamics.

For the lowest density contrast case ($\eta = 0.01$), the jet is highly under-dense compared to the ambient medium. It shows rapid deceleration and strong interaction with the surroundings, as seen in Figure 18(a). The density field indicates that the initially light jet core is quickly compressed and displaced, with the jet head located close to the inlet at approximately $x \sim 0.3$. The large cocoon region filled with shocked ambient material and backflow is enclosed by a broad bow shock formed ahead of the jet head. There is a strong reduction in axial velocity downstream, along with significant transverse motion, with v_y reaching approximately ± 0.3. This leads to substantial lateral spreading, with the jet width increasing from the initial radius of 0.05 to more then 0.30, as reflected in the mixing-layer evolution in Figure 20(a). Due to the strong velocity gradient and low inertia of the jet, Kelvin–Helmholtz instability develops prominently along the shear layer producing visible distortions and enhanced mixing. The relativistic effects weaken quickly in this case as the Lorentz factor decreases rapidly downstream.

The jet maintains a more stable structure while still interacting with the ambient medium for density contrast of $\eta = 0.1$ as shown in Figure 18(b). The jet head reaches approximately $x \sim 0.6$ and the jet core remains visible over a longer distance. Compared to the highly under-dense case the bow shock becomes more localized and clearly defined and the cocoon region is narrower. While transverse velocity components reduce to approximately $v_y \sim \pm 0.15$, the axial velocity remains relatively high over a larger portion of the domain. The jet spreads less compared to the $\eta = 0.01$ case with a reduced but consistent mixing over the domain as seen in Figure 20(b).

Kelvin–Helmholtz instability develops more gradually and remains mainly confined to the outer shear layer. Compared to the lower density case the Lorentz factor also remains higher along the jet axis for a longer distance, indicating improved momentum transport.

For the highest density contrast ($\eta = 0.5$) from Figure 18, the jet becomes significantly more stable and penetrates much further into the domain. In Figure 18 (c), the jet head reaches approximately $x \sim 0.9$. The density field shows a well-defined and continuous jet core with a relatively sharp boundary separating it from the ambient medium. The bow shock is strong and sharply curved, located far downstream. The cocoon region is smaller compared to the lower density cases. The axial velocity remains close to its injection value, approximately $v_x \sim 0.99$, across most of the domain and transverse velocities are strongly reduced, remaining approximately less than 0.05. Kelvin–Helmholtz instability is much weaker in this case, with minimal distortion along the shear layer. The Lorentz factor remains high along the jet axis, indicating sustained relativistic motion.

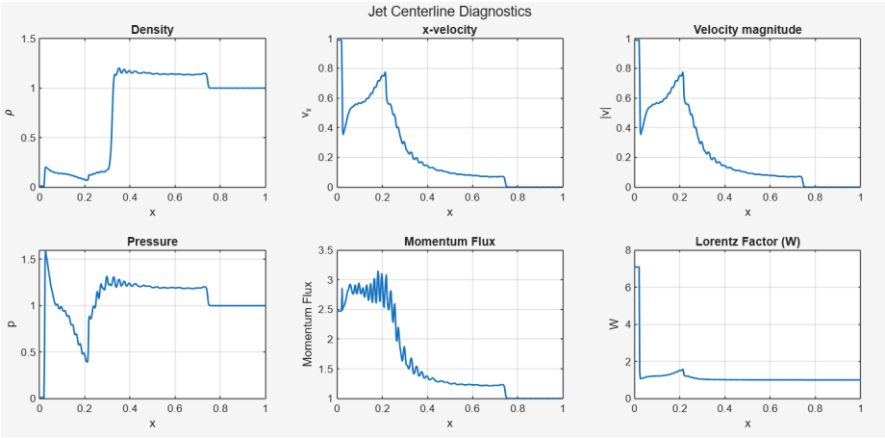

a) $\eta = 0.01$

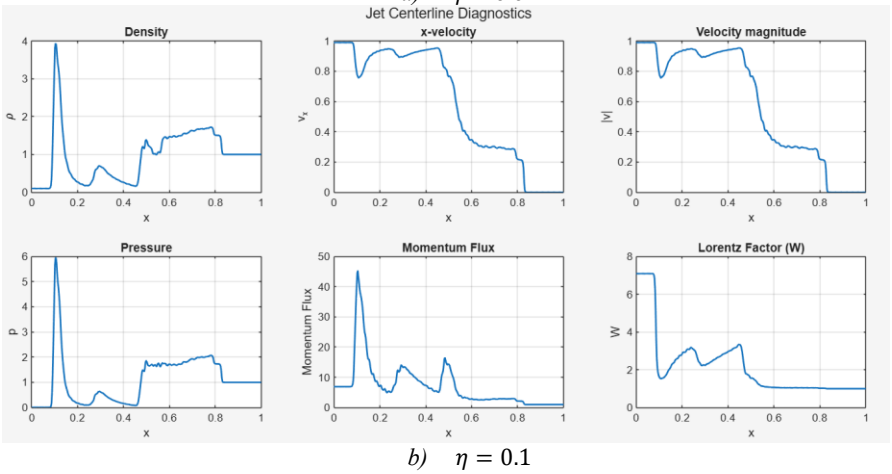

b) $\eta = 0.1$

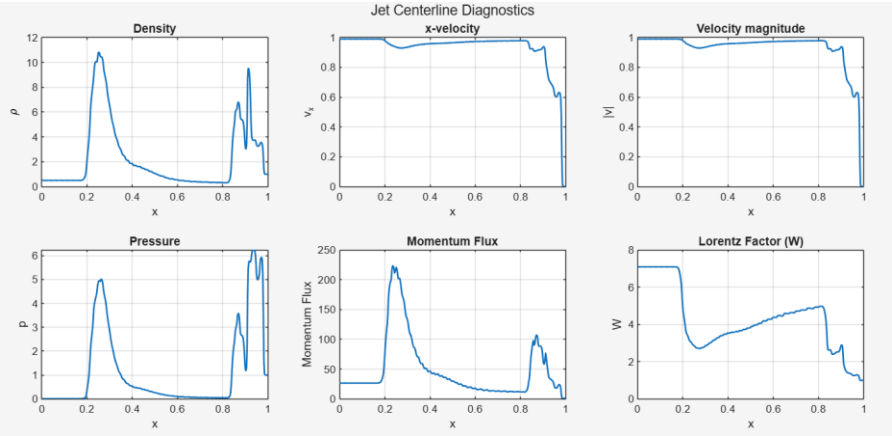

c) $\eta = 0.5$

Figure 19:Centerline profiles illustrating the effect of density contrast on jet dynamics.

The centerline profiles shown in Figure 19 highlight the evolution of axial properties for each case. For $\eta = 0.01$, the density rapidly increases toward ambient values, the axial velocity drops significantly, and the Lorentz factor approaches unity within a short distance, indicating strong mixing and loss of jet features. For $\eta = 0.1$, these changes occur more gradually, and the jet core remains identifiable over a longer region. For $\eta = 0.5$, the density remains relatively low compared to the ambient medium, the axial velocity stays high, and the Lorentz factor remains elevated across most of the domain.

Figure 20 show that the jet penetration length increases from approximately 0.30 for $\eta = 0.01$, to about 0.6 for $\eta = 0.1$, and nearly 0.9 for $\eta = 0.5$. The bow shock position also moves further downstream as density contrast increases. At the same time, the mixing of the layers of jet and the surrounding takes place further into the domain with the increase value of density contrast, indicating greater resistance in mixing and stronger jet stability.

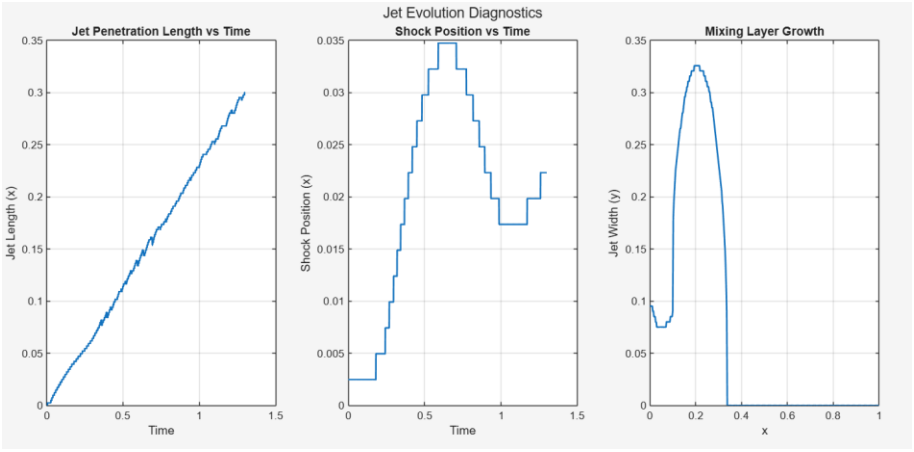

a) $\eta = 0.01$

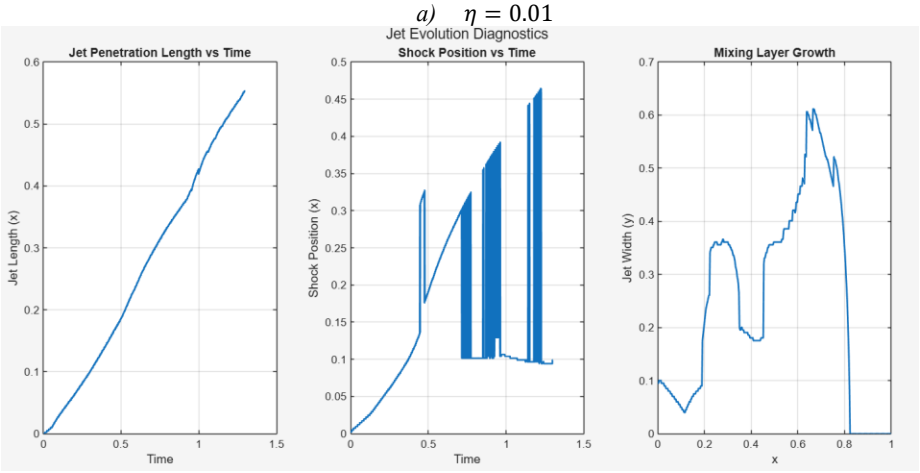

b) $\eta = 0.1$

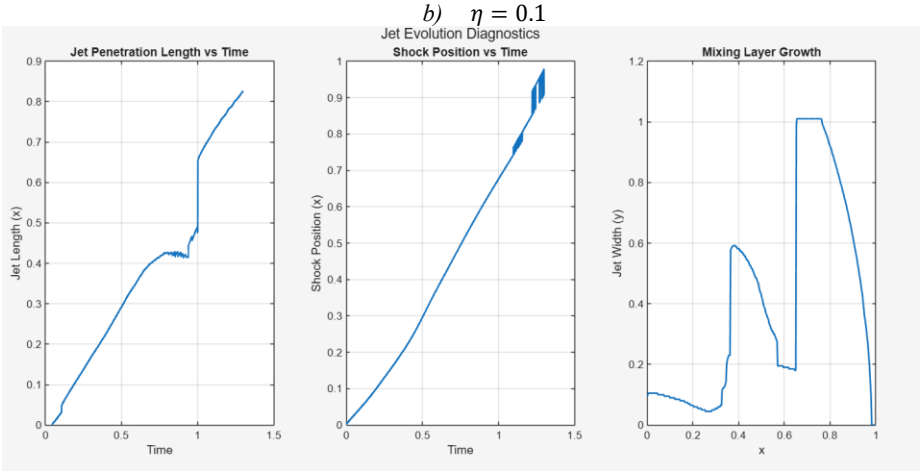

c) $\eta = 0.5$

Figure 20: Jet evolution diagnostics showing effect of density contrast on jet dynamics.

The results clearly show that density contrast plays a key role in controlling jet behavior. Lower the density contrast stronger is the interaction with ambient medium which lead to rapid spreading

and mixing. With increase in jet density limited is the lateral spreading and instability growth leading to narrower and more stable jet.

4.5.3 Effects of Pressure Ration on Jet Dynamics

Figures 21–23 illustrate the effects of pressure ratio on relativistic jet dynamics for three cases corresponding to $p_j/p_a = 0.01$, 1, and 5. A jet is injected from the left boundary at $y = 0.5$ with radius $r_j = 0.05$ in a two-dimensional domain $[0,1] \times [0,1]$. The jet properties are $\rho_j = 0.1$, $v_x = 0.99$, $v_y = 0$, and varying pressure $p_j = 0.01, 1, 5$, while the ambient medium is at rest with $\rho_a = 1$, $p_a = 1$. Adiabatic index $\Gamma = 4/3$ is taken. The results demonstrate the influences of pressure imbalance in jet structure, stability, and propagation.

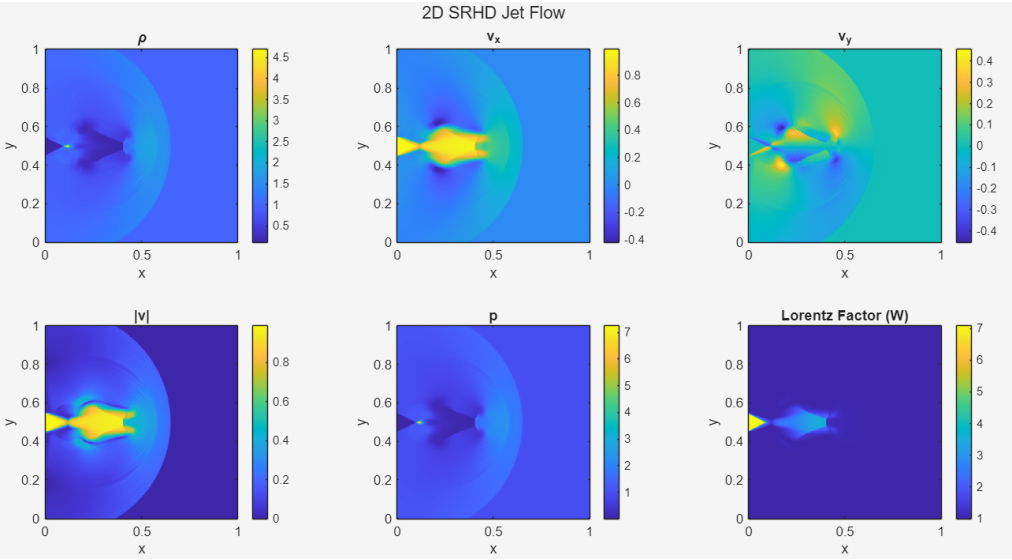

a) $p_j / p_a = 0.01$

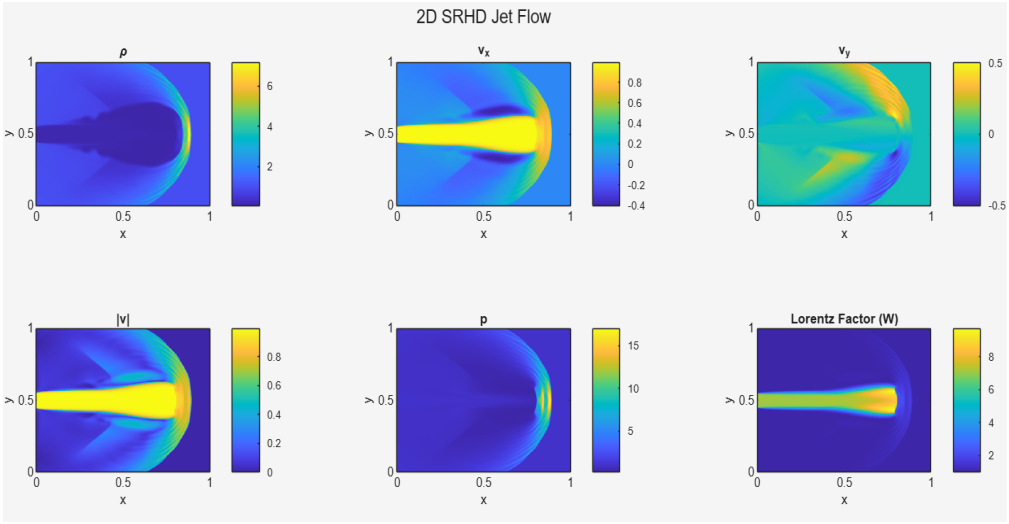

b) $p_j / p_a = 1$

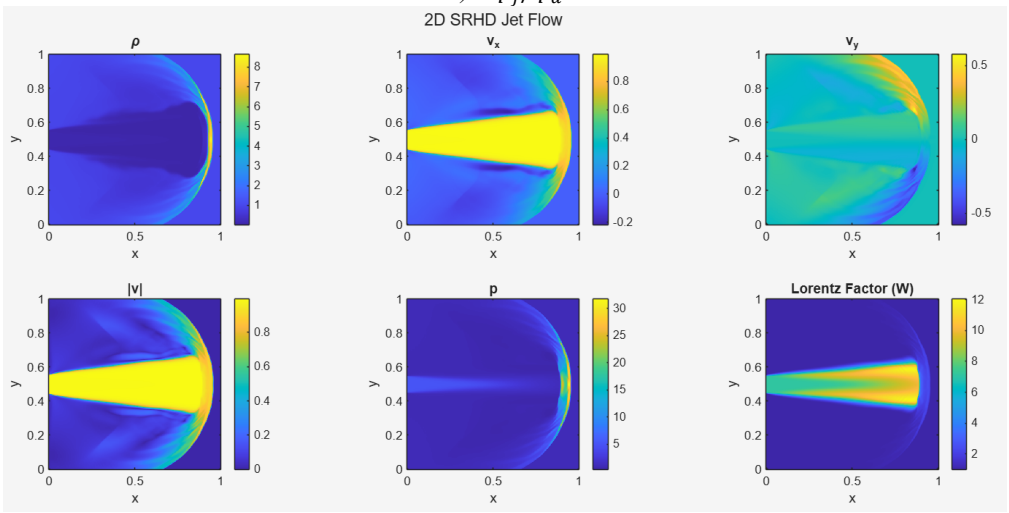

c) $p_j / p_a = 5$

Figure 21: Effect of pressure ratio on jet dynamics.

Figure 21(a) for the under-pressured case $\left(p_j/p_a = 0.01\right)$ shows the jet undergoes immediate lateral compression after injection due to the higher ambient pressure. Within a short downstream distance, the jet core narrows rapidly and loses coherence. The axial velocity drops to approximately below 0.2 from the injected value by $x \approx 0.5$. The Lorentz factor reduces to values close to unity, as observed in the centerline profiles in Figure 22(a). Due to the weak internal support, the pressure field shows a rapid adjustment toward ambient conditions. Strong transverse motions develop and v_y reaches approximately ±0.4, leading to a thick shear layer and enhanced mixing. The jet structure breaks down early as the Kelvin–Helmholtz instability grows rapidly and dominates the flow evolution. The bow shock remains weak and diffuse. Figure 23(a) shows that

the jet penetration length is limited to approximately $x \approx 0.45$. The jet is unstable and dissipates its momentum quickly due to compression and mixing.

In the second case with a match in pressure of jet and ambient medium $\left(p_j/p_a = 1\right)$, the jet exhibits stable and efficient propagation. The jet maintains a well-collimated structure with a low-density core extending downstream as shown in Figure 21(b). The axial velocity remains high and close to the injected value, and the Lorentz factor is also sustained over a significant distance, as seen in Figure 22(b). Ahead of the jet head, a distinct bow shock forms and a surrounding cocoon region develops due to the accumulation of shocked jet and ambient material. It helps maintain the jet structure with an additional confinement. Except for near the jet head the transverse velocities remain small due to reduced lateral disturbances and suppressed instability growth. The velocity and momentum transport are largely preserved with only gradual variation as shown by the centerline profiles. Compared to the under-pressured case, the jet penetrates significantly farther and reaches approximately $x \approx 0.8$, with a steadily advancing shock front, as shown in Figure 23(b). This case of jet propagation is momentum-driven.

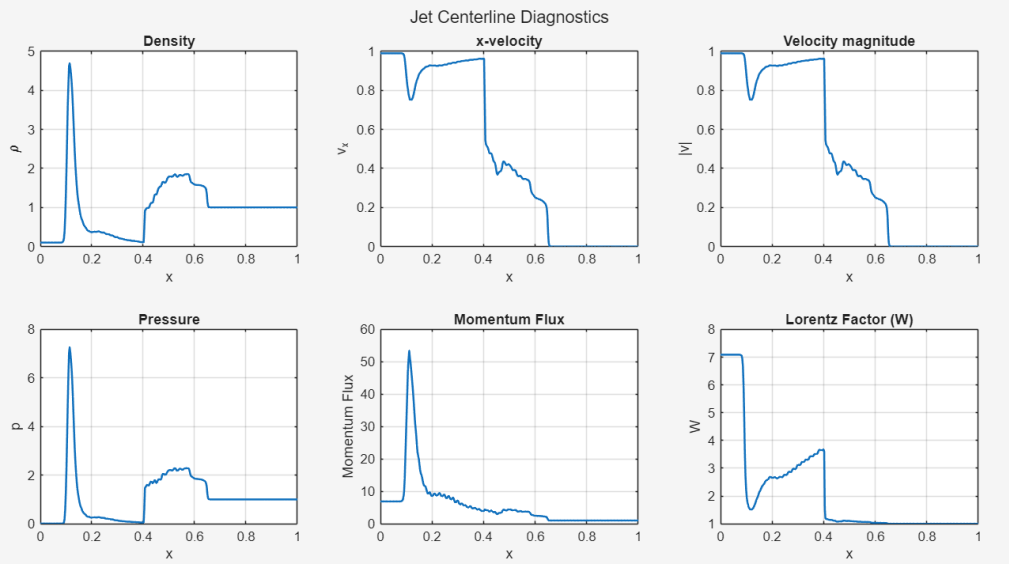

a) $p_j/\,p_a = 0.01$

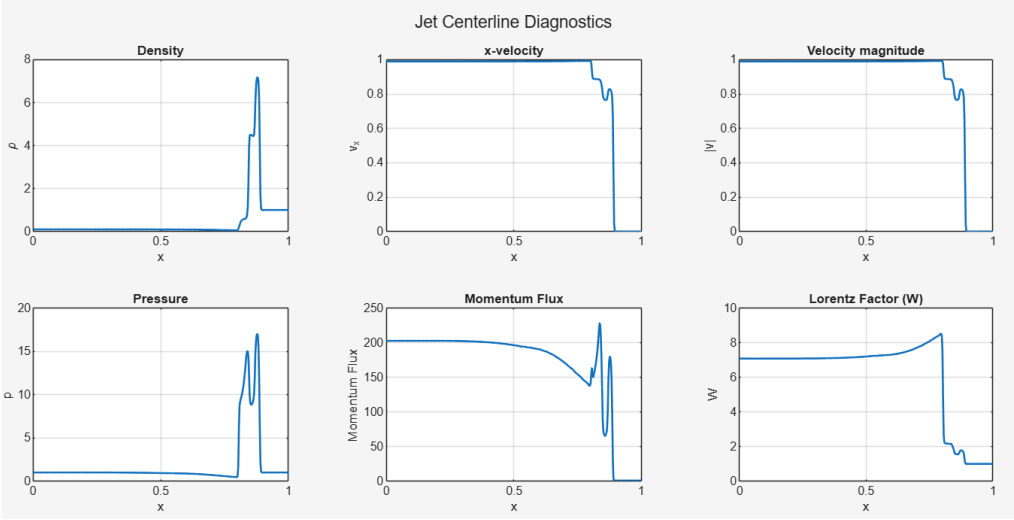

b) $p_j / p_a = 1$

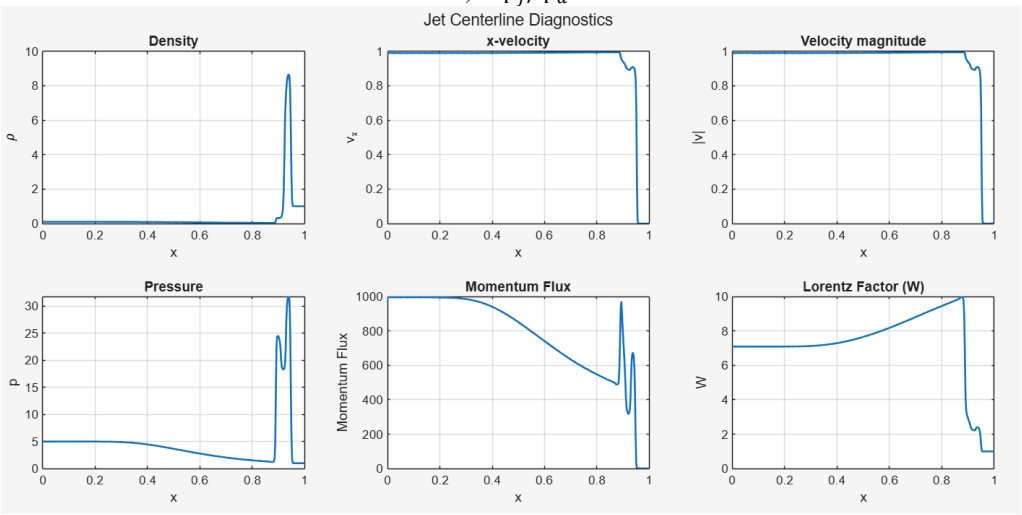

c) $p_j / p_a = 5$

Figure 22: Centerline profiles illustrating the effect of pressure ratio on jet dynamics.

For the over-pressured jet case $\left(p_j/p_a = 5 \right)$, the jet dynamics are dominated by strong expansion followed by recollimation. There is an initial widening of the jet near the inlet, visible in Figure 21(c). The excess internal pressure drives rapid lateral expansion which is followed by compression as the jet interacts with the surrounding medium. It produces alternating expansion and compression regions along the axis. These appear as oscillatory structures in the velocity and pressure fields and correspond to internal shock patterns. Figure 22(c) shows that the Lorentz factor reaches higher values compared to the other cases. A strong bow shock forms near the jet head, and a high-pressure cocoon surrounds the jet. The jet remains coherent and propagates

efficiently, reaching approximately $x \approx 1$, as shown in Figure 23(c) even in the presence of internal oscillations. The mixing layer initially increases due to expansion but stabilizes downstream.

The jet evolution diagnostics in Figure 23 further highlights these differences. The jet penetration length increases from approximately 0.45 in Figure 23(a) to above 0.8 in Figure 23(b) and over 0.9 in Figure 23(c). With the increase in pressure ratio, the bow shock position advances faster. Due to strong instability the jet mixes with ambient medium rapidly in under-pressured case. In matched pressure case it is moderate and in over-pressured case initially there is large mixing of layers but later it stabilizes.

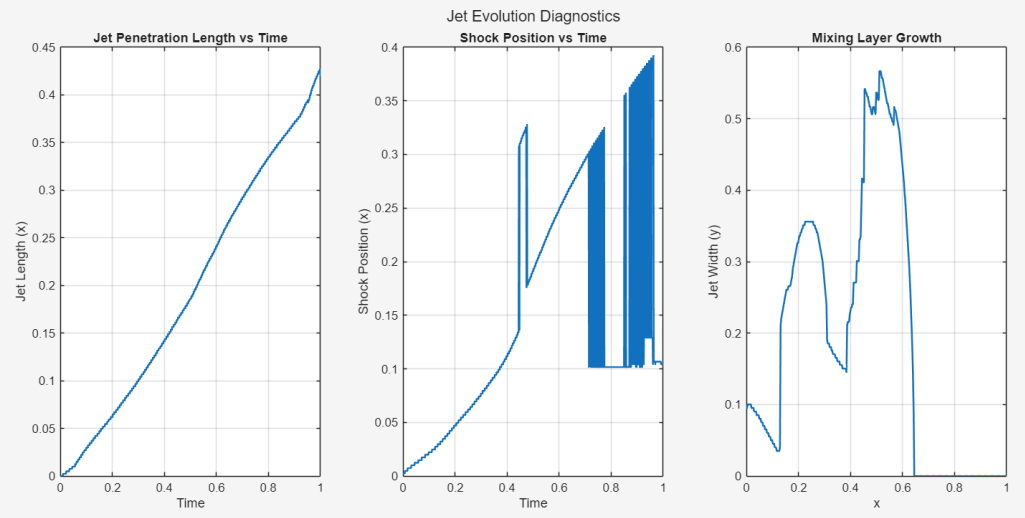

a) $p_j / p_a = 0.01$

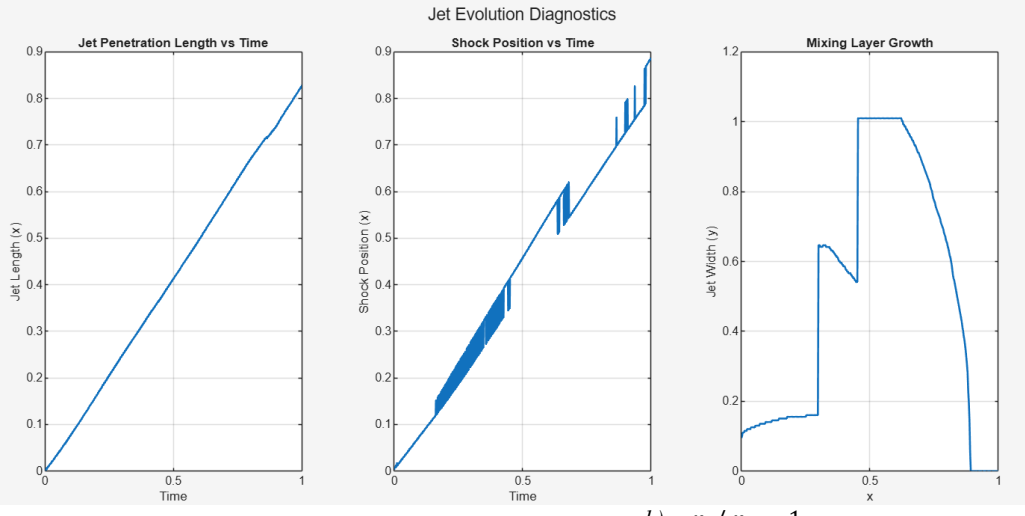

b) $p_j / p_a = 1$

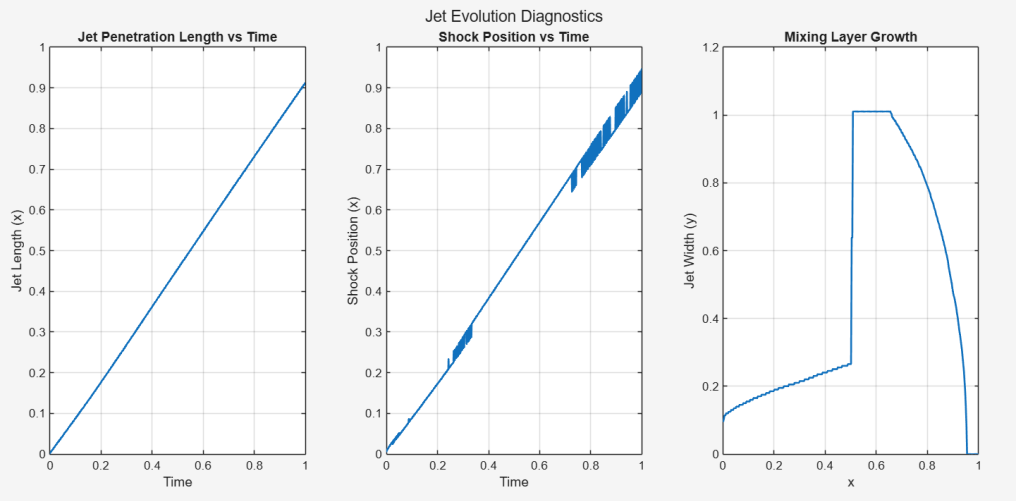

c) $p_j / p_a = 5$

Figure 23: Jet evolution diagnostics showing effect of pressure ratio on jet dynamics.

Overall, the pressure ratio helps determine if the jet is dominated by compression, balanced propagation, or expansion-driven dynamics. The under-pressured jet is unstable and quickly disrupted, the pressure-matched jet remains stable and efficiently propagating, and the over-pressured jet develops internal oscillatory structures while maintaining strong forward motion.

4.6 High-Resolution Numerical Simulation of SRHD Jet Flow

The jet propagation was simulated on a higher-resolution 800 × 800 grid to examine how spatial refinement influences the resolved relativistic jet structures. The computational domain, initial conditions, and boundary conditions remain the same as in the baseline simulation (Figures 13–15), while the final simulation time is taken as $t = 1$ to ensure that the evolving jet structure remains within the computational domain.

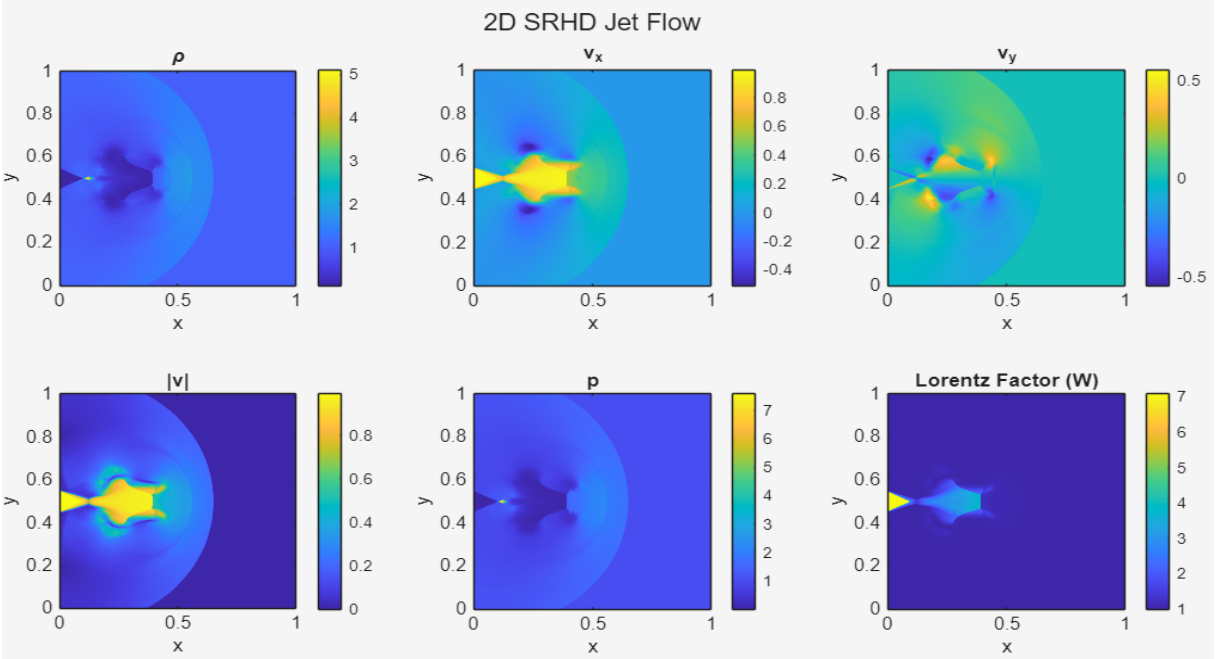

Figure 24: Field visualization of high-resolution jet simulation with uniform 800 × 800 grids.

The field visualization in Figure 24 shows a narrow, high-velocity jet emerging from the left boundary and propagating along the x-direction. Near the inlet the jet maintains a well-defined core. There is a clear contrast between the low-density jet and the surrounding ambient medium. In comparison to the 400 × 400 case (Figure 12), the jet boundaries here appear sharper, and there is more distinctly resolved interface between the jet and ambient medium. The flow is enclosed within a shock envelope by a curved bow shock. A high-pressure cocoon develops due to the accumulation of shocked jet and ambient fluid inside this region. The spatial variations and internal structures of the cocoon that were less distinct in the coarser grid is clearly visible in this case of comparatively higher resolution.

Along the jet axis, appearing as a sequence of high- and low-pressure zones are the alternating compression and expansion regions. These correspond to internal shocks and expansion regions that arise due to pressure mismatch between the jet and the surrounding medium. These features are more clearly defined and exhibit a more continuous pattern along the jet core at higher resolution. The axial velocity remains dominant along the centerline, while transverse velocity components develop along the jet boundary. These transverse motions indicate the growth of shear-

driven instabilities and they are more clearly resolved compared to the lower-resolution simulation and hence appear as small-scale distortions along the jet interface.

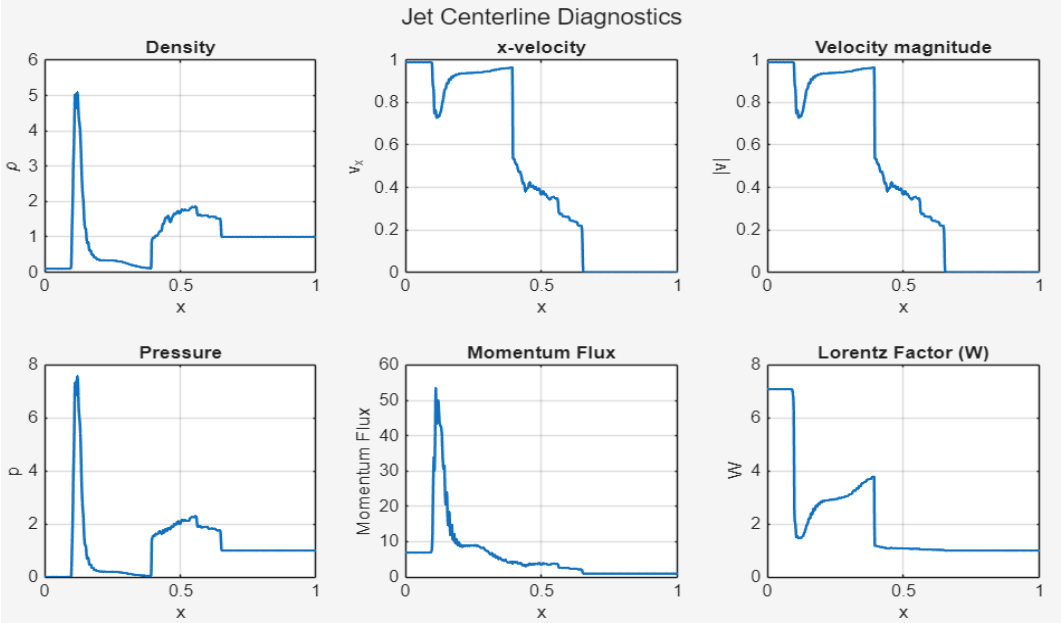

Figure 25: Centerline profiles of relativistic jet of 800 × 800 uniform grid.

One-dimensional representation of the jet evolution along the axis is provided by the centerline profiles in Figure 25. Sharper transitions near compression regions are visible in the density and pressure profiles, indicating improved resolution of shock structures. The axial velocity remains high near the inlet and gradually decreases downstream due to interaction with the ambient medium. The Lorentz factor is elevated in the jet core and decreasing in regions affected by shocks and mixing. The momentum flux profile shows reduced smoothing of peaks and gradients compared to the 400 × 400 case (Figure 13) and has a clearer variation along the axis, indicating improved resolution of momentum transport.

The effect of spatial refinement is further illustrated by the jet evolution diagnostics in Figure 26. With the sustained forward propagation of the jet head, the jet penetration length has increased steadily over time. The shock position reflects the interaction between internal structures, cocoon dynamics, and the advancing jet front with noticeable variations. The mixing layer growth shows a more detail along the streamwise direction, capturing the development of the shear layer with

greater clarity than in the lower-resolution case (Figure 14). The instability-driven mixing clearly shows regions of rapid growth and local variation in jet width with the help of stronger resolution.

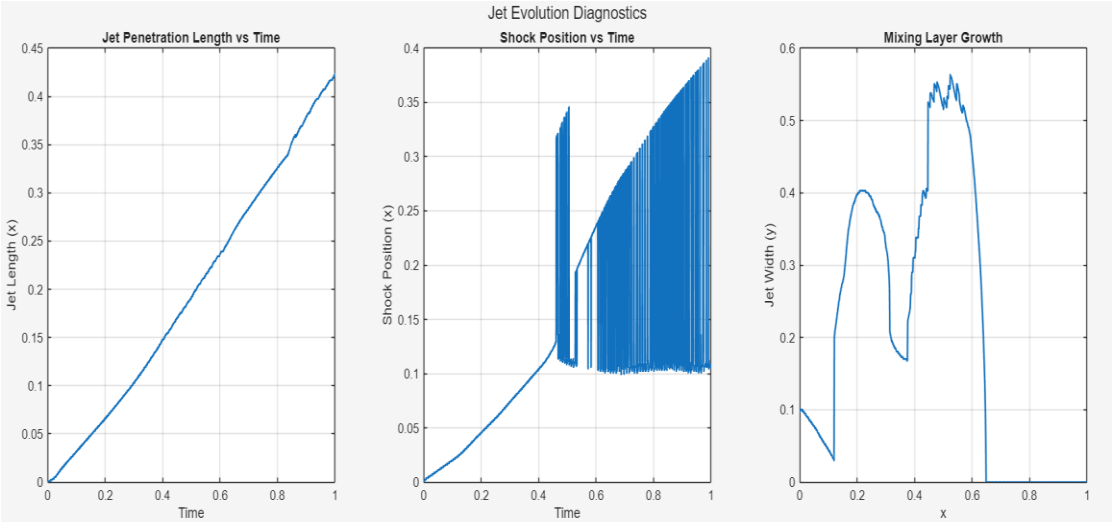

Figure 26: Jet evolution diagnostics of relativistic jet of 800 × 800 uniform grid.

Higher the grid resolution lower is the numerical diffusion which allows finer flow features to be captured. Shock structures appear sharper, internal jet features are more clearly defined, and the development of shear-layer instabilities becomes more visible all while the general jet morphology remains consistent with the lower-resolution simulation.

However, finer mesh enforces a smaller time step through the CFL condition and significantly increases the number of required flux evaluations, MUSCL reconstructions, and primitive variable recoveries at each iteration. This increases the simulation time and require higher memory, making the high-resolution configuration computationally expensive, particularly for extended runs or multiple parametric studies. Thus, the 800×800 simulation provides a more detailed and physically accurate depiction of jet dynamics with an introduction of practical limitation in terms of computational feasibility.

5. CONCLUSION

In conclusion reduced dimensional (1D and 2D) SRHD solver using a finite volume framework with HLLE flux along with piecewise constant and MUSCL reconstruction with slope limiting approach were successfully developed and validated it against standard relativistic blast wave problems, demonstrating accurate capture of rarefaction waves, contact discontinuities, and shock structures along with strong conservation properties. The developed solver can recover primitive variables almost as accurately as exact solvers with L_1, L_2 and $L\infty$ errors ranging from ~0.04 to ~3 for density and from ~0.004 to ~0.9 for velocity. For pressure L_1 and L_2 error were in the range of ~0.03 to around 10 while $L\infty$ error was approximately 85. The extension to two dimensions preserved the correctness of the solution and was further validated through planar shock tests and circular blast wave simulation, which proved the solver's ability to handle multidimensional relativistic flows with stability and symmetry.

The application of the validated 2D solver to study relativistic jet propagation demonstrated the formation of a collimated jet core, bow shock, and shear layer, with centerline and evolution diagnostics capturing axial momentum transport, shock dynamics, and mixing behavior. Results from parametric studies showed that higher Lorentz factors enhance jet collimation and stability, higher density contrast improves inertial resistance to mixing, and pressure ratio governs the initial expansion or compression behavior of the jet. Increased grid resolution improved the accuracy of shock and interface representation but resulted in significantly higher computational cost. The variation in CFL value influenced the stability of the solver but it has very little effect on the improvement of the solution accuracy.

Overall, the developed solver provides a reliable and physically consistent framework for simulating relativistic hydrodynamic phenomena.

6. FUTURE ENHANCEMENT

Future work can focus on reducing numerical diffusion and enhancing the resolution of sharp discontinuities and small-scale instabilities using of higher-order numerical schemes such as WENO or PPM. For improving the accuracy of contact discontinuity capturing, more advanced Riemann solvers, such as HLLC can be incorporated.

To enable more realistic representation of jet dynamics, particularly for studying inherently three-dimensional instabilities and turbulent mixing, the solver can be extended to three-dimensional (3D) configuration. Additionally, adaptive mesh refinement (AMR) techniques can be implemented to provide high resolution in critical regions such as shock fronts and shear layers while maintaining computational efficiency.

Magnetic fields can be included through relativistic magnetohydrodynamics (RMHD) that would significantly enhance the applicability of the solver to astrophysical jets, where magnetic effects play a crucial role in jet collimation and stability. Further, in order to capture energy loss mechanisms, radiative processes can be executed.

Finally, the increased computational cost associated with high-resolution and multi-dimensional simulations can be addressed with the parallelization of the solver using high-performance computing techniques, enabling extensive parametric studies.

REFERENCES

[1] Rezzolla, Luciano, and Olindo Zanotti, *Relativistic Hydrodynamics* (Oxford, 2013; online edn, Oxford Academic, 23 Jan. 2014), https://doi.org/10.1093/acprof:oso/9780198528906.001.0001, accessed 3 Apr. 2026.

[2] Diver, D.A. (1992) 'Relativistic Fluids and Magneto-Fluids. By A. M. ANILE. Cambridge University Press, 1990. 400 pp. £50.', *Journal of Fluid Mechanics*, 238, pp. 723–724. doi:10.1017/S0022112092221881.

[3] Martí, J.M., Müller, E. Grid-based Methods in Relativistic Hydrodynamics and Magnetohydrodynamics. *Living Rev Comput Astrophys* **1**, 3 (2015). https://doi.org/10.1007/lrca-2015-3

[4] Font, J.A. Numerical Hydrodynamics and Magnetohydrodynamics in General Relativity. *Living Rev. Relativ.* **11**, 7 (2008). https://doi.org/10.12942/lrr-2008-7

[5] Jin Matsumoto, Youhei Masada, Propagation, cocoon formation, and resultant destabilization of relativistic jets, *Monthly Notices of the Royal Astronomical Society*, Volume 490, Issue 3, December 2019, Pages 4271–4280, https://doi.org/10.1093/mnras/stz2821

[6] Kaye, C. D., Cawthorne, T. V., & Hughes, P. A. (2018). Hydrodynamical Simulations of Recollimation Shocks within Relativistic Astrophysical Jets. *Galaxies*, *6*(2), 53. https://doi.org/10.3390/galaxies6020053

[7] Mizuta, A., Yamada, S., & Takabe, H. (2004). Propagation and dynamics of relativistic jets. *The Astrophysical Journal*, *606*(2), 804-818.

[8] Martí, J.M., Müller, E. Numerical Hydrodynamics in Special Relativity. *Living Rev. Relativ.* **6**, 7 (2003). https://doi.org/10.12942/lrr-2003-7

[9] Mignone, A., & Bodo, G. (2005). An HLLC Riemann solver for relativistic flows—I. Hydrodynamics. *Monthly Notices of the Royal Astronomical Society*, *364*(1), 126-136.

[10] Martı, J. M., & Müller, E. (1996). Extension of the piecewise parabolic method to one-dimensional relativistic hydrodynamics. *Journal of Computational Physics*, *123*(1), 1-14.

[11] Jamie F Townsend, Shu-ichiro Inutsuka, László Könözsy, Karl W Jenkins, On high-order numerical schemes for viscous relativistic hydrodynamics through the Kelvin–Helmholtz instability, *Monthly Notices of the Royal Astronomical Society*, Volume 515, Issue 1, September 2022, Pages 451–472, https://doi.org/10.1093/mnras/stac1741

[12] Alessandro Lupi, A general relativistic extension to mesh-free methods for hydrodynamics, *Monthly Notices of the Royal Astronomical Society*, Volume 519, Issue 1, February 2023, Pages 1115–1131, https://doi.org/10.1093/mnras/stac3574

[13] Dönmez, O. (2006). Solving 1-D special relativistic hydrodynamics (SRH) equations using different numerical methods and results from different test problems. *Applied mathematics and computation*, *181*(1), 256-270.

[14] Martí, J. M., & Müller, E. (1994). The analytical solution of the Riemann problem in relativistic hydrodynamics. *Journal of Fluid Mechanics*, *258*, 317-333.

[15] Sod, G. A. (1978). A survey of several finite difference methods for systems of nonlinear hyperbolic conservation laws. *Journal of computational physics*, *27*(1), 1-31.

[16] Martı, J. M., & Müller, E. (1999). High-Resolution Shock-Capturing Methods in Relativistic Hydrodynamics. *Living Reviews in Relativity*, 2(3).

[17] Schneider, V., Katscher, U., Rischke, D. H., Waldhauser, B., Maruhn, J. A., & Munz, C. D. (1993). New algorithms for ultra-relativistic numerical hydrodynamics. *Journal of Computational Physics*, *105*(1), 92-107.

[18] Einfeldt, B. (1988). On Godunov-type methods for gas dynamics. *SIAM Journal on numerical analysis*, *25*(2), 294-318.

[19] Harten, A., Lax, P. D., & Leer, B. V. (1983). On upstream differencing and Godunov-type schemes for hyperbolic conservation laws. *SIAM review*, *25*(1), 35-61.

[20] Toro, E. F., Spruce, M., & Speares, W. (1994). Restoration of the contact surface in the HLL-Riemann solver. *Shock waves*, *4*(1), 25-34.

[21] Mignone, A., Plewa, T., & Bodo, G. (2005). The piecewise parabolic method for multidimensional relativistic fluid dynamics. *The Astrophysical Journal Supplement Series*, *160*(1), 199-219.

[22] Zhang, W., & MacFadyen, A. I. (2006). RAM: A relativistic adaptive mesh refinement hydrodynamics code. *The Astrophysical Journal Supplement Series*, *164*(1), 255-279.

[23] Van Leer, B. (1979). Towards the ultimate conservative difference scheme. V. A second-order sequel to Godunov's method. *Journal of computational Physics*, *32*(1), 101-136.

[24] Guercilena, F., Radice, D., & Rezzolla, L. (2017). Entropy-limited hydrodynamics: a novel approach to relativistic hydrodynamics. *Computational Astrophysics and Cosmology*, *4*(1), 3.

[25] Mignone, A., Bodo, G., Massaglia, S., Matsakos, T., Tesileanu, O. E., Zanni, C., & Ferrari, A. (2007). PLUTO: a numerical code for computational astrophysics. *The Astrophysical Journal Supplement Series*, *170*(1), 228-242.

[26] Stone, J. M., Tomida, K., White, C. J., & Felker, K. G. (2020). The athena++ adaptive mesh refinement framework: Design and magnetohydrodynamic solvers. *The Astrophysical Journal Supplement Series*, *249*(1), 4.

[27] Radice, D., Rezzolla, L., & Galeazzi, F. (2014). High-order fully general-relativistic hydrodynamics: new approaches and tests. *Classical and Quantum Gravity*, *31*(7), 075012.

[28] Pons, J. A., Marti, J. M., & Müller, E. (2000). The exact solution of the Riemann problem with non-zero tangential velocities in relativistic hydrodynamics. *Journal of Fluid Mechanics*, *422*, 125-139.

[29] Rezzolla, L., & Zanotti, O. (2001). An improved exact Riemann solver for relativistic hydrodynamics. *Journal of Fluid Mechanics*, *449*, 395-411.

त्रिभुवन विश्वविद्यालय
TRIBHUVAN UNIVERSITY
इन्जिनियरिङ्ग अध्ययन संस्थान
INSTITUTE OF ENGINEERING
पुल्चोक क्याम्पस
PULCHOWK CAMPUS
Accredited by University Grants Commission (UGC) Nepal 2020
5-521260
5-521611
5-522104
5-522809
पुल्चोक, ललितपुर।
Pulchowk, Lalitpur

त्रिभुवन विश्वविद्यालय
इन्जिनियरिङ्ग अध्ययन संस्थान
पुल्चोक क्याम्पस

Date: May 9, 2026

To Whom It May Concern:

This is to certify that the paper titled "*Development and Validation of a One-Dimensional SRHD Solver Using HLLE Riemann Scheme and MUSCL Reconstruction for Relativistic Blast Wave Problems*" (Submission ID #1130), with **Dikshya Kafle** as the first author, was accepted through the peer-review process and has been presented at the 18th IOE Graduate Conference, organized at Pulchowk Campus, Lalitpur, Nepal, from May 7 to 9, 2026.

Please note that inclusion of the accepted manuscript in the conference proceedings is contingent upon timely compliance with any further editorial requirements during the publication process.

Prof. Sangeeta Singh
Convener
18th IOE Graduate Conference

Dikshya Kafle

SRHD_Dikshya kafle_Plag check.pdf

Tribhuvan University

Document Details

Submission ID
trn:oid:::3117:586950638

Submission Date
May 6, 2026, 1:00 PM GMT+5:45

Download Date
May 6, 2026, 1:08 PM GMT+5:45

File Name
SRHD_Dikshya kafle_Plag check.pdf

File Size
4.5 MB

75 Pages

14,882 Words

88,632 Characters

18th May 2026

5% Overall Similarity

The combined total of all matches, including overlapping sources, for each database.

Filtered from the Report

- Bibliography
- Quoted Text
- Cited Text
- Small Matches (less than 8 words)

Custom Section Exclusions

{titlesCount} Section Titles, {keywordsCount} Keywords

Section title	No. of Section Starters	Section Starters
"Acknowledgements"	4	Acknowledgements, Acknowledgement, Acknowledgment, Acknowledgments

Match Groups

- **80** Not Cited or Quoted 5%
  Matches with neither in-text citation nor quotation marks
- **0** Missing Quotations 0%
  Matches that are still very similar to source material
- **0** Missing Citation 0%
  Matches that have quotation marks, but no in-text citation
- **0** Cited and Quoted 0%
  Matches with in-text citation present, but no quotation marks

Top Sources

3% Internet sources
4% Publications
0% Submitted works (Student Papers)

Integrity Flags

0 Integrity Flags for Review

No suspicious text manipulations found.

Our system's algorithms look deeply at a document for any inconsistencies that would set it apart from a normal submission. If we notice something strange, we flag it for you to review.

A Flag is not necessarily an indicator of a problem. However, we'd recommend you focus your attention there for further review.

Match Groups

- 80 Not Cited or Quoted 5%
  Matches with neither in-text citation nor quotation marks
- 0 Missing Quotations 0%
  Matches that are still very similar to source material
- 0 Missing Citation 0%
  Matches that have quotation marks, but no in-text citation
- 0 Cited and Quoted 0%
  Matches with in-text citation present, but no quotation marks

Top Sources

3% Internet sources
4% Publications
0% Submitted works (Student Papers)

Top Sources

The sources with the highest number of matches within the submission. Overlapping sources will not be displayed.

1	Publication	
Naseem Uddin. "Computational Fluid Dynamics - Numerical Methods and Applica...		<1%
2	Internet	
link.springer.com		<1%
3	Internet	
www.science.gov		<1%
4	Internet	
www.semanticscholar.org		<1%
5	Internet	
ir.busitema.ac.ug		<1%
6	Publication	
M. E. Feyz, M. R. Nalim, V. R. Hasti, J. P. Gore. "Modeling and Analytical Solution of ...		<1%
7	Internet	
www.researchgate.net		<1%
8	Internet	
repository.tudelft.nl		<1%
9	Publication	
Donat, R.. "A Flux-Split Algorithm Applied to Relativistic Flows", Journal of Compu...		<1%
10	Internet	
amsdottorato.unibo.it		<1%

11	Internet epub.ub.uni-greifswald.de	<1%
12	Internet hdl.handle.net	<1%
13	Publication Manuel Hernández Marco. "A non-linear quasi-3D model for air management mo...	<1%
14	Publication David L. Meier. "Black Hole Astrophysics", Springer Science and Business Media L...	<1%
15	Publication Eleuterio F. Toro. "Computational Bodily Fluid Dynamics", Springer Science and B...	<1%
16	Internet www.osti.gov	<1%
17	Publication A. Mignone. "The Piecewise Parabolic Method for Multidimensional Relativistic Fl...	<1%
18	Publication Shuta J Tanaka, Kenji Toma. "Efficient acceleration of cylindrical jets: effects of ra...	<1%
19	Publication Shide Tan, Lijun Hu, Haizhuan Yuan. "Development of a Shock-Stable and Contact...	<1%
20	Internet rosap.ntl.bts.gov	<1%
21	Internet spiral.imperial.ac.uk	<1%
22	Publication Eliot H Ayache, Hendrik J vanEerten, Frédéric Daigne. "Late X-ray flares from the l...	<1%
23	Publication Kunlei Zhao, Yulong Du, Li Yuan. "A New Sixth-Order WENO Scheme for Solving H...	<1%
24	Publication Kyanjo, Brian. "GeoFlood: Computational Model for Overland Flooding", Boise Sta...	<1%

25	Internet	
	ir.msu.ac.zw:8080	<1%
26	Publication	
	D. A. Shirobokov. "Third-Order Accurate Conservative Method on a Unstructured ...	<1%
27	Publication	
	Saeid Eslamian, Faezeh Eslamian. "Flood Handbook - Analysis and Modeling", CRC...	<1%
28	Internet	
	mediatum.ub.tum.de	<1%
29	Internet	
	putnam.lib.udel.edu	<1%
30	Internet	
	www.humehealth.com.au	<1%
31	Internet	
	www.tandfonline.com	<1%
32	Publication	
	David Radice, Luciano Rezzolla. "Discontinuous Galerkin methods for general-rela...	<1%
33	Publication	
	José A. Font. "Numerical Hydrodynamics in General Relativity", Living Reviews in ...	<1%
34	Internet	
	aries.res.in	<1%
35	Internet	
	biblio.ugent.be	<1%
36	Internet	
	elibrary.tucl.edu.np	<1%
37	Internet	
	pastel.archives-ouvertes.fr	<1%
38	Internet	
	umpir.ump.edu.my	<1%

39	Internet	
	www.nature.com	<1%
40	Internet	
	www.numerik.mathematik.uni-mainz.de	<1%
41	Publication	
	"Compact Objects in Astrophysics", Springer Nature, 2007	<1%
42	Internet	
	68ea08c8-6bd5-4fda-ae85-daf9ce8fa9ed.filesusr.com	<1%
43	Publication	
	Causon, D.. "A Cartesian cut cell method for shallow water flows with moving b...	<1%
44	Publication	
	Causon, D.. "Calculation of shallow water flows using a Cartesian cut cell approac...	<1%
45	Publication	
	José Maria Martí, Ewald Müller. "Numerical Hydrodynamics in Special Relativity", ...	<1%
46	Publication	
	Masud Chaichian, Ioan Merches, Daniel Radu, Anca Tureanu. "Electrodynamics", ...	<1%
47	Publication	
	Ramanbhai, Patel Manojbhai. "Numerical Investigation of Fluid Flow in Lid-Driven...	<1%
48	Publication	
	Walg, S., A. Achterberg, S. Markoff, R. Keppens, and Z. Meliani. "Relativistic AGN je...	<1%
49	Internet	
	deepai.org	<1%
50	Internet	
	worldwidescience.org	<1%